




Article

Comparative Study of Sulfides from Porphyry, Skarn, and Carbonate-Replacement Mineralization at the Recsk Porphyry-Mineralized Complex, Hungary

Máté Biró¹, Johann G. Raith² , Monika Feichter², Máté Hencz¹, Gabriella B. Kiss¹ , Attila Virág³ and Ferenc Molnár^{1,*} 

- ¹ Institute of Geography and Earth Sciences, Department of Mineralogy, ELTE Eötvös Loránd University, 1053 Budapest, Hungary; mate.biro@ttk.elte.hu (M.B.); gabriella.b.kiss@ttk.elte.hu (G.B.K.)
² Chair of Resource Mineralogy, Department of Applied Geosciences and Geophysics, Montanuniversität Leoben, 8700 Leoben, Austria
³ Institute of Geography and Earth Sciences, Department of Petrology and Geochemistry, ELTE Eötvös Loránd University, 1053 Budapest, Hungary
* Correspondence: molnar.ferenc@ttk.elte.hu

Abstract: A calc–alkaline dioritic–andesitic–dacitic intrusive–volcanic complex of Early Oligocene (30 Ma) age and its Mesozoic sedimentary basement at Recsk host a well-preserved porphyry–skarn–polymetallic carbonate-replacement–epithermal mineral system. The unique occurrence offers an exceptional possibility to study these related mineralization types at a single locality. This study presents the textural–paragenetic, compositional characteristics, and systematics of sulfide mineral assemblages for the porphyry, skarn, and carbonate-replacement ore types, which are currently situated at a depth of 500–1200 m below the present surface. Detailed petrography combined with EPMA analyses of molybdenite, galena, sphalerite, tetrahedrite-group minerals and Bi-bearing sulfosalts allows for the establishment of characteristic mineral and chemical fingerprints for each mineralization type. Rhenium concentration in molybdenite, occurring as rare disseminations and quartz–carbonate veinlets in altered host rocks in all three mineralization types, shows a decreasing trend towards the more distal mineralization types. High Re contents ($\bar{x} = 1.04$ wt.%, max. up to 4.47 wt%) are typical for molybdenite from the porphyry mineralization, but Re is not homogeneously distributed, neither within individual molybdenite crystals nor on a mineralization scale. Copper and Se show opposite behavior in molybdenite, both becoming enriched in the more distal mineralization types. Silver, Bi, and Se concentrations increase in galena and tetrahedrite-group minerals, both towards the country rocks, making them the best candidates for vectoring within the whole hydrothermal system. For tetrahedrite-group minerals, Ag, Bi, Se, together with Sb and Zn, are the suitable elements for fingerprinting; all these are significantly enriched in the distal carbonate-replacement mineralization compared to the other, more proximal ore types. Additionally, further trends can be traced within the composition of sulfosalts. Lead-bearing Bi sulfosalts preferentially occur in the polymetallic carbonate-replacement veins, while being under-represented in the skarn and porphyry mineralization. Porphyry mineralization hosts Cu-bearing Bi sulfosalts dominantly, while skarn is characterized by Bi-dominated sulfosalts. Sphalerite, although present in all mineralization types, cannot be used for fingerprinting, vectoring, or thermobarometry based on EPMA measurements only. Trace element contents of sphalerite are low, often below the detection limits of the analyses. This is further complicated by the intense “chalcopyrite disease” occurring throughout the distal mineralization types. All the above-listed major, minor, and trace element ore mineral characteristics enable the characterization of the Recsk ores by mineral geochemical fingerprints, providing a possible vectoring tool in porphyry Cu–(Mo)–Au-mineralized systems.

Keywords: porphyry; sulfide; EPMA; fingerprinting; vectoring; skarn; carbonate replacement



Citation: Biró, M.; Raith, J.G.; Feichter, M.; Hencz, M.; Kiss, G.B.; Virág, A.; Molnár, F. Comparative Study of Sulfides from Porphyry, Skarn, and Carbonate-Replacement Mineralization at the Recsk Porphyry-Mineralized Complex, Hungary. *Minerals* **2024**, *14*, 956. <https://doi.org/10.3390/min14090956>

Academic Editors: Chao Yang, Yiwei Peng and Gangyang Zhang

Received: 23 August 2024
Revised: 16 September 2024
Accepted: 19 September 2024
Published: 21 September 2024



Copyright: © 2024 by the authors. Licensee MDPI, Basel, Switzerland. This article is an open access article distributed under the terms and conditions of the Creative Commons Attribution (CC BY) license (<https://creativecommons.org/licenses/by/4.0/>).

1. Introduction

Porphyry copper deposits provide the majority of the worldwide Cu ore production and are important sources of Mo and Au [1]. The increasing demand for copper caused by the green energy transition [2,3] calls for evolved methods of exploration for this type of mineral system. The porphyry Cu(–Mo–Au)-style mineralization at the subvolcanic level of intrusive–volcanic complexes is a part of a larger-scale mineral system in which skarn, carbonate-replacement, sedimented-hosted distal-disseminated, subepithermal vein-style, and intermediate- and high-sulfidation epithermal ore types may also occur. Preservation of all of those ore types within a single system is rarely seen. The intrusive–volcanic complex of Paleogene age at Recsk provides an excellent opportunity to study porphyry and associated ore systems. This is due to the fact that all of the different mineralization types with common origin at subvolcanic and volcanic levels listed above are known and explored within a small area [4–13].

Mineral trace element fingerprints are widely used to describe the genetic framework and further economic potential of ore deposits [14–17]. Trace element distributions can also be used for mineral exploration purposes, as trace element contents of various mineral phases may change with changing geochemical conditions typical for different mineralizing conditions [18–21]. Sphalerite is widely used for thermobarometry [22,23], molybdenite is well-known for its Re content [1,24–26], and tetrahedrite-group minerals may also provide an effective tool for fingerprinting/vectoring within various mineralization types [13,14,27,28], although galena and sulfosalts are less often used for these purposes in porphyry Cu mineralization.

In this paper, we present results of detailed textural and paragenetic observations combined with electron microprobe (EPMA) data for ore minerals from the porphyry, skarn, and carbonate-replacement mineralization types in the Recsk ore complex. These data interpreted together are appropriate to describe the distribution and zoning of metals and minor elements in ore minerals within the whole mineralized Recsk area, which may provide a further fingerprinting tool applicable for refining ore system models and vectoring towards different types of ores in the diorite porphyry-related mineralized system.

Geology and Mineralization of the Intrusive–Volcanic Complex at the Recsk

The intrusive–volcanic complex of the Paleogene (Early Oligocene) age at Recsk is a part of a metallogenic belt that extends from the western Central Alps at Traversella in Italy eastward as far as Recsk in NE Hungary [10,29–32] along the Insubrian–Periadriatic–Middle-Hungarian Line (Figure 1).

At Recsk, diorite intrusion and associated mineralization systems at subvolcanic levels are not exposed on the surface; they became known from extensive drilling and underground exploration activities that were completed from the late 1950s to early 1990s in the 20th century. Dioritic bodies (stocks and veins) of around 29 Ma age [33] intruded Mesozoic sediments and are overlain by volcanic, volcano–sedimentary, and sedimentary rocks of the Late-Eocene–Early-Oligocene age [4,7,33–36]. The intrusive and volcanic rocks of the Paleogene age show subduction-related, medium-to-high-K calc-alkaline geochemical characteristics and form a single unit within the Paleogene Volcanic Belt of Hungary [10,29,37]. Diorite stocks intruded Jurassic olistostromes, predominantly containing Triassic to Jurassic sedimentary units (limestone, dolomite, chert) and less widespread basaltic rocks [7,36]. The Mesozoic basement is overlain by Late Eocene–Early Oligocene sedimentary rocks (limestone, marl, clay) [33] which are overlain and crosscut by the extrusive and intrusive volcanic units of the ore complex. The Cu–porphyry mineralization is hosted by the diorite stocks and their endoskarn zones along their deep-seated contacts with the Mesozoic sedimentary units (Figure 2), with indicated resources of 781 Mt Cu-ore (0.66% Cu, 0.4% cut-off with 0.005% Mo and 0.28 g/t Au) and 159 Mt Cu-ore (1.16% Cu, 0.01% Mo and 0.17 g/t Au), respectively [38–40].

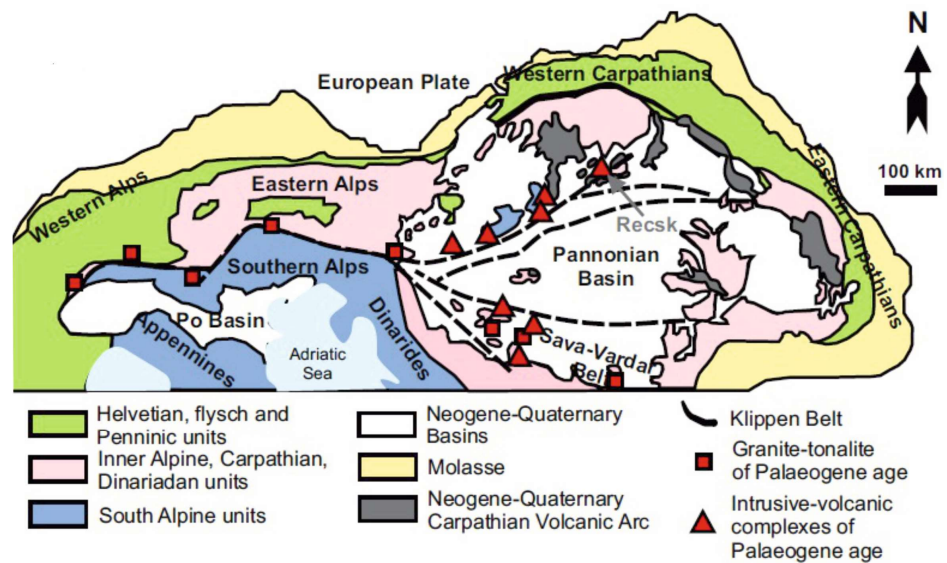


Figure 1. Geological setting of the mineralized Recsk complex along the Insubrian–Periadriatic–Middle-Hungarian line. Note the Paleogene volcanic and intrusive complexes occurring along the tectonic line, their northeastern-most exposure being Recsk. Modified after Molnár 2007.

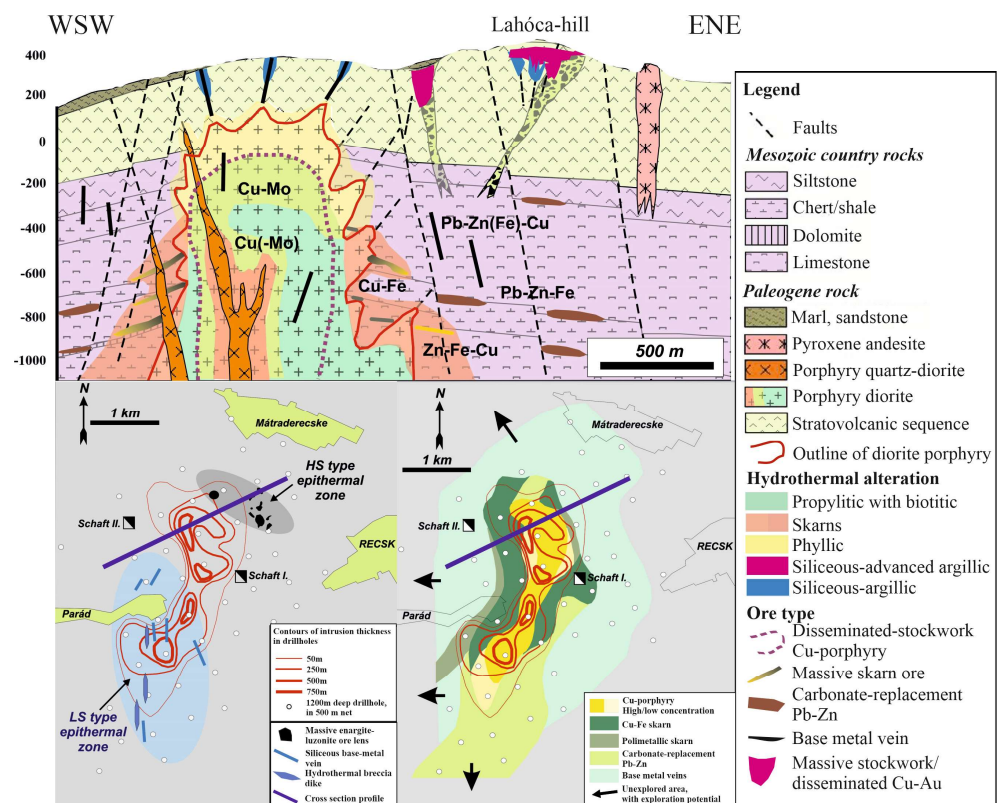


Figure 2. Cross-section and contour maps of the mineralized Recsk complex. Multiple apexes of the complex diorite porphyry can be seen on both the cross-section and the contour maps. Mineralized zones extend as far as 2 km from the porphyry diorite, showing a Cu–Zn–Pb metal zonation trend towards the country rocks. Epithermal zones are situated within the stratovolcanic units, hosted by diatreme breccias and tectonically preformed zones. Based on [7,10,12].

The main porphyry orebody is surrounded by skarns along its contact with the Mesozoic sedimentary rocks (Figure 2), containing horizontally and vertically zoned Cu–

Zn–Pb mineralization with 36 Mt Cu-ore (2.19% Cu) and 11.5 Mt Zn-ore (4.98% Zn). In the zones towards the country rocks, the Triassic–Jurassic tectonically disturbed units host a polymetallic Zn–Pb carbonate-replacement ore with grades as high as 3.15–3.5% Zn and 1.2–2.1% Pb locally [40,41].

The shallow epithermal zones of the Recsk ore complex have been targeted by mining and intense exploration since the early 19th century, but mining of the Cu–Au ore was stopped in the 1970s. In the past 20–30 years, Brownfield mineral exploration has mostly targeted the epithermal Cu–Ag–Au intermediate sulfidation (IS) and Cu–Au high-sulfidation (HS)-type ore zones at shallow depths, above the porphyry stocks (Figure 2) [8,13]. Those exploration programs reported an indicated remaining resource of 32.4 Mt of Au ore with 1.47 g/t of average-grade Au in the HS-type mineralization zones [38].

2. Materials and Methods

2.1. Samples

Based on the results of previous studies on more than 500 samples, a total of 32 samples were selected for the purpose of this study, all of which were accessible from the drill core sample repository of the Department of Mineralogy, Eötvös Loránd University, Budapest (Table 1). The selected samples represent the three deep-seated economically significant mineralization types, i.e., Cu(–Mo–Au) porphyry, Cu, and Zn–Pb skarn and Pb–Zn–(Ag) carbonate replacement mineralization. The selected sample set represents both the rocks from the northernmost part of the mineralization as well as the more southern intrusives and their surroundings. Samples were selected upon mineral composition, preferring those that contain measurable crystals from most of the studied mineral species. Some samples derive from the archive collection of representative drill cores from the mineralization.

Table 1. Drill core samples used for petrography and EPMA studies from the northern intrusive part of the Recsk mineralization. Ore types: PO–Cu–(Mo)–Au-porphyry, SK-skarn, CAR–polymetallic carbonate replacement. Minerals: py—pyrite, cpy—chalcopyrite, fhl—tetrahedrite-group minerals, sph—sphalerite, ga—galena, sphs—sulfosalt, mo—molybdenite, sch—scheelite, va—vallerite, to—tochilinite, mt—magnetite.

Drillcore	Spl. Nr.	Coordinates (WGS 84)			Mineralogy		Mineralization Type
		X	Y	Z	Ore Minerals	Gangue Minerals	
Rm-30	63	47.9349	20.0694	−290.3	py, cpy, fh, ga, sphs	fs, qz, ag,	PO
Rm-30	64	47.9349	20.0694	−400.6	py, ga, sph, sphs, mo	qz, fs, ag, cc, dol	PO-CAR
Rm-34	05	47.9373	20.0615	−602.3	py, sph, ga, cpy, sphs	qz, cc	CAR
Rm-34	06	47.9373	20.0615	−697.3	py, sph, sphs, fhl	qz, cc	CAR
Rm-34	07	47.9373	20.0615	−716.3	py, mo, sch, sph, fhl, sphs	dol, qz,	CAR
Rm-34	42	47.9373	20.0615	−796.3	py, sph, cpy, fhl, sphs, sch, mo	qz, grt	SK
Rm-34	43	47.9373	20.0615	−818.3	py, sphs, sch, cpy	qz	SK
Rm-34	44	47.9373	20.0615	−832.8	py, sphs, sch, cpy	fs, qz, ag	PO
Rm-34	46	47.9373	20.0615	−961.3	py, fhl, sphs	fs, qz, ag	PO
Rm-35	5	47.9359	20.0658	−337.8	py, cpy, sph, ga, sphs	fs, qz, ag	PO
Rm-35	6	47.9359	20.0658	−334.3	py, cpy, sph, ga	fs, qz, ag	PO
Rm-35	7	47.9359	20.0658	−373.8	py, mo, cpy, ga, fhl	fs, qz, ag, cc	PO
Rm-35	8	47.9359	20.0658	−372.8	py, mo, fhl, sph,	fs, qz, ag, cc	PO
Rm-35	13	47.9359	20.0658	−569.3	py, mo, cpy	fs, qz, ag, cc	PO
Rm-35	16	47.9359	20.0658	−677.3	py, mo, cpy	fs, qz, ag, cc	PO
Rm-35	17	47.9359	20.0658	−682.8	py, mo	fs, qz, ag	PO
Rm-35	21	47.9359	20.0658	−782.3	py, mo	fs, qz, ag	PO
Rm-35	23	47.9359	20.0658	−786.3	py, mo, cpy, sphs	qz, grt, px	SK

Table 1. Cont.

Drillcore	Spl. Nr.	Coordinates (WGS 84)			Mineralogy		Mineralization Type
		X	Y	Z	Ore Minerals	Gangue Minerals	
Rm-35	24	47.9359	20.0658	−837.3	py, mo, cpy	fs, qz, ag	PO
Rm-45	340	47.9329	20.0709	−839.3	py, cpy, mo,	qz, amf	SK
Rm-61	01	47.9420	20.0625	−664.5	py, sph, cpy, ga, sphs	qz, cc, dol, fl	CAR
Rm-63	03	47.9324	20.0604	−506.3	py, ga, sph, sphs	cc	CAR
Rm-64	01	47.9280	20.06202	−233.0	py, sph, ga, fhl, sphs	qz, cc, dol	CAR
Rm-70	01	47.9203	20.0698	−576.9	py, sph, ga, cpy	cc, px, ag	SK
Rm-70	16	47.9203	20.0698	−313.3	py, cpy, mo, ga	fs, qz, ag	PO
Rm-71	74	47.9172	20.0580	−926.9	py, cpy, ga, sph, sphs	cc, qz, anh	SK
Rm-71	499	47.9172	20.0580	−907.0	py, sph, ga, cpy, sphs	grt, qz, px, cc	SK
Rm-71	02	47.9203	20.0698	−717.9	py, sph, ga, cpy	px, ep, srp, cc	SK
Rm-73	49	47.9186	20.0631	−58.3	py, cpy, mo, sph, ga, sphs	fs, qz, ag	PO
Rm-77	492	47.92569	20.0633	−219.3	py, po, mt, sph, ga, to, va, ala	grt, anh, br	SK
Rm-82	516	47.9021	20.0513	−645.2	py, sph, ga, cpy	anh	SK
Rm-87	01	47.9368	20.0557	−422.3	py, sph, ga, fhl, cpy	qz, cc	CAR

2.2. Methods

Microscopic studies were performed on 30 or 100 µm thick polished thin sections. Optical microscopy was performed with a Zeiss Axioplan polarization microscope equipped with Zeiss AxioCam 208 camera (Carl Zeiss GmbH, Jena, Germany). Scanning electron microscopic (SEM) imaging was implemented using an AMRAY 1830i electron microscope with a PU9800 energy-dispersive detector at the Eötvös Loránd University, Institute of Geography and Earth Sciences, and a Thermo Scientific PhenomXL Desktop SEM, equipped with a CeB₆ electron source and a built-in SDD energy-dispersive spectrometer, provided by AuroScience Ltd (Budapest, Hungary).

Electron microprobe (EPMA) measurements of sulfide minerals were performed on a JEOL JXA-8200 WD/ED-combined microanalyzer at the Eugen F. Stumpfl Electron Microprobe Laboratory at Montanuniversität Leoben. Measurement conditions for all analyses were 20 kV acceleration voltage and 10 nA sample current. Standardization was made with SPI Supplies natural and artificial CuFeS₂, ZnS, HgS, PtAs, MoS₂, CuS, PbS, BiAgSe₂, Sb₂S₃, SnS₂, PdTe sulfide; V, Ge, Cd, In, and Re pure metals; and Mn₅Si₅O₁₅ silicate reference materials. EPMA measurements were performed on sphalerite, galena, tetrahedrite, molybdenite, Bi-sulfosalts, and kesterite. The elements measured in sphalerite were the following: Zn, S, Fe, Mn, Cu, Cd, Hg, Ge, In, V; in galena: Pb, S, Ag, Se, Bi, Cu; in tetrahedrite-group minerals: As, Sb, S, Fe, Zn, Cu, Ag, Te, Se, Bi, Hg, Pb, Cd, Se; in molybdenite: Mo, S, Se, Re, Cu, W; in bismuth sulfides: Bi, S, Pb, Cu, Se, Te, Ag, and Sn; and in kesterite: Zn, V, Fe, Cu, S, Se, In, Cd, Mn. Individual measurements, measurement conditions, times, and detection limits for each element are listed in the electronic appendix.

Data analysis was performed in IMDEX ioGAS and R software environment (version 4.3.1; [42]).

3. Results

3.1. Petrography

3.1.1. Porphyry Cu–(Mo)–Au Ore

The porphyry-copper-type mineralization is mostly hosted by the apical zones of the diorite intrusion, but mineralized zones extend subordinately in the endoskarn rock assemblage as well. The Cu–Mo ore is contained mostly by a quartz-rich stockwork zone in the diorite, while the endoskarns are characterized by lenticular ore bodies with massive-to-disseminated Cu mineralization [5].

The porphyry mineralization is characterized by a 50–150 m thick zone of intensively altered rock assemblage hosting stockwork Cu(–Mo–Au) mineralization. K-metasomatic zones are often overprinted by various degrees of propylitic or phyllic alteration (Figure 2),

resulting in the presence of sericite/illite together with quartz, or green sheet-silicate minerals accompanied by epidote. The primary porphyry minerals plagioclase and amphibole are often replaced by quartz–illite–sulfide paragenesis or chlorite–quartz–sulfide–apatite paragenesis. All the mineralized samples are characterized by intense veining. Veins are characterized according to Sillitoe [43]. M-type veins were not observed, but multiple generations of A-, B-, and D-type veins are widespread in the studied samples. These veins are also accompanied by multiple generations of carbonate veins. While A-type veins are characteristically present in the potassic alteration zone, B-type and D-type veins tend to occur within variously altered samples even within the surrounding endoskarns. Carbonate veins with various mineralogy are present throughout the entire mineralized porphyry stock.

The stockwork mineralization is characterized by the mineralogically and genetically diverse veinlets cross-cutting each other, which are the most important carriers of the sulfide ore minerals. As samples come from 63.5 mm halved drill cores, clear cross-cutting relations cannot always be determined, thus multiple generations of the same vein type are not necessarily distinguishable. There are early, exclusively cellular or, more rarely, sugary quartz veins, quartz–sulfide veins, which typically contain pyrite, rarely chalcopyrite, galena, iron oxide, or K-feldspar, in addition to quartz. These are recognized as A-type veins, and by their mineralogy and appearance, at least two different generations can be distinguished. These two types of A-type veins are distinguished by their sulfide mineral contents. There are veins hosting exclusively pyrite, while in other A-type vein generations, other sulfide minerals may also occur, although only in subordinate amounts. A-type veins may occur throughout the mineralized system, their thickness being mostly between 2 and 30 mm.

Multiple generations of B-type veins can be distinguished by their mineralogy. There are mainly quartz–pyrite veins, but quartz–pyrite–chalcopyrite, quartz–pyrite–molybdenite veins and quartz–pyrite–chalcopyrite–molybdenite veins can also be recognized as subclasses of B-type veins (Figure 3e). Sulfide minerals usually occur in the central parts of these veins, but there are veins which show multiple sequences and/or asymmetrical distribution of ore minerals; these latter veins have a banded texture. When B-type veins crosscut mafic porphyry phenocrysts, massive sulfide replacement of the phenocryst usually occurs (Figure 3c,d), forming a “sulfide-bead” laced up on the narrow (1–5 mm) quartz–sulfide vein. B-type veins occur both in the mineralized diorite apices and the surrounding endoskarns. B-type veins in the endoskarns typically crosscut the original textural features of the rocks such as remaining sedimentary structures, mineral nodules, or massive sulfide lenses. Thickness of B-type veins typically range between 1 and 5 mm.

D-type veins with their typical sericite–illite-rich alteration halos and relatively higher sulfide contents are also abundant. Besides the quartz–sericite–sulfide veins, some pure sulfide (pyrite, chalcopyrite) veins may also be categorized to type-D based on their cross-cutting relations. Besides their dominantly pyrite–chalcopyrite ore mineral assemblage, molybdenite or, rarely, scheelite may also occur within some of these veins. Repeated “bands” of quartz–sulfide parageneses in some veins also suggest multiple re-opening processes. Carbonates also occur as central zones of D-type veins, typically with a calcite–dolomite, pyrite, chalcopyrite, \pm molybdenite, galena mineralogy (Figure 3f).

Within the apical and outermost lying parts of the diorite intrusion, but sometimes also within the K-metasomatic zones, multiple generations of carbonate veins can be observed. These are usually thicker (generally 5–40 mm) than the usual B- and D-type veins and banded even within the porphyry mineralization center. These carbonate veins often show a banded texture. The wall rock usually shows sericitic, or propylitic, alteration. The veins generally start with coarse-grained drusy quartz, followed by quartz, pyrite, chalcopyrite, molybdenite, and galena mineral assemblages, followed by the precipitation of carbonates and sericite. Pyrite, molybdenite, and galena tend to occur in the central carbonate part of the veins too.

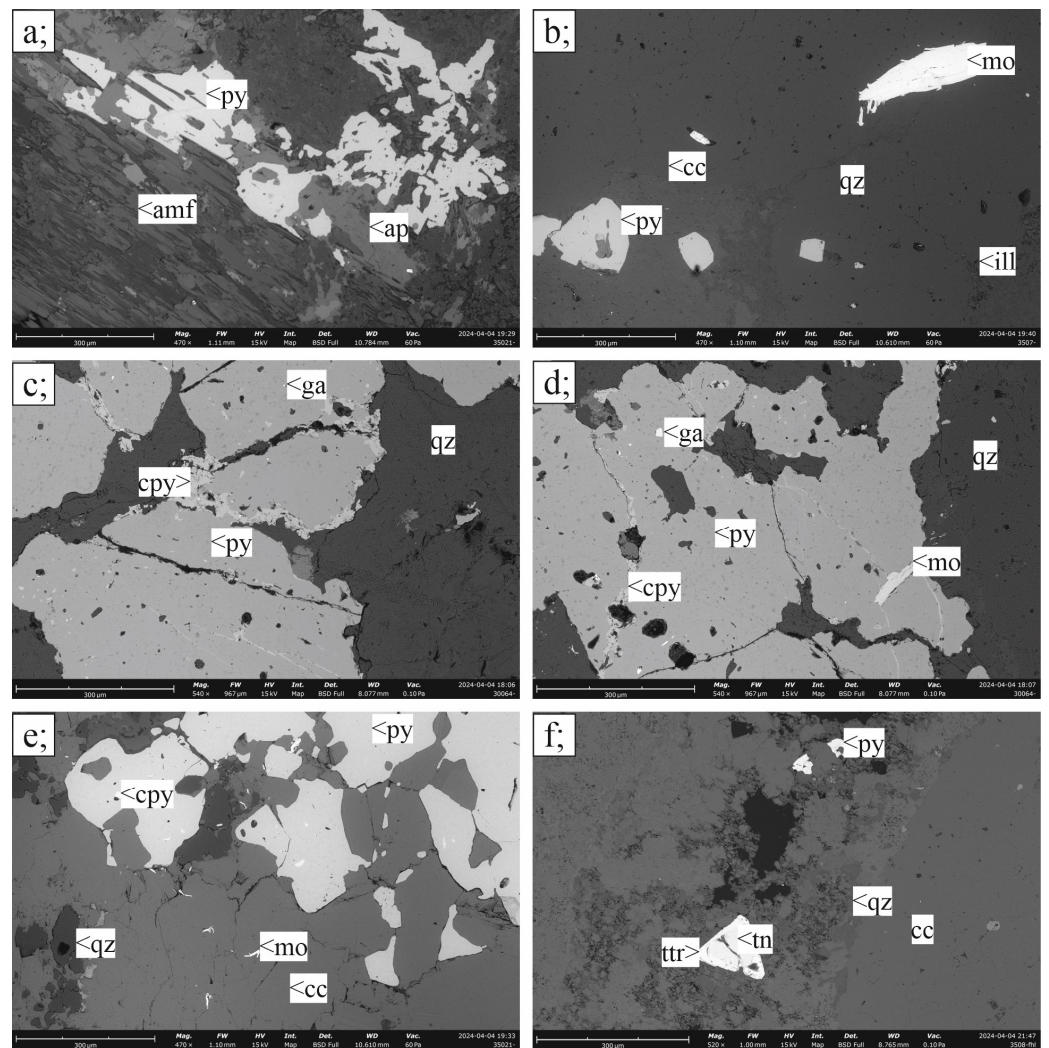


Figure 3. Ore textures on SEM-BSE images from the Cu–(Mo)–Au mineralization: (a), replacement of magmatic amphibole grain (amf) by chlorite and skeletal pyrite (py) with apatite (ap) at the rims (Rm35–21); (b), euhedral pyrite and subhedral molybdenite (mo) “fish” within carbonate(cc)–quartz(qz)–illite(ill) vein with baddeleyite (Rm35–07); (c), anhedral porphyry pyrite replacing glomeroporphyritic nodule with chalcopyrite inclusions, crosscut by galena-bearing chalcopyrite veins (Rm30–64); (d), sulfide paragenesis replacing tabular porphyry phenocryst. Molybdenite and galena (ga) inclusions in anhedral porphyry pyrite, crosscut by chalcopyrite veins (Rm30–64); (e), anhedral pyrite in quartz vein with rounded chalcopyrite (cpy) inclusions associated with thin flakes of molybdenite embedded in quartz (Rm35–16); (f), euhedral tennantite (tn) with Sb-enriched tetrahedrite rim (ttr) associated with pyrite in quartz–illite porphyry matrix (Rm35–08).

Carbonate veins are classified into several additional types based on their mineral association: (1) quartz–carbonate–pyrite veins with pyrite being the one and only sulfide, (2) carbonate veins with molybdenite–pyrite–chalcopyrite–galena characteristic mineral association (Figure 3b), (3) quartz–carbonate–pyrite–molybdenite–tennantite veins, and (4) sphalerite–galena–pyrite-bearing carbonate veins containing chalcopyrite and abundant sulfosalts too. In addition, quartz, anhydrite, barite, celestite, clay minerals—typically illite—may appear in any of the above-mentioned carbonate veins. Minor monazite, rare earth carbonates like bastnäsite, apatite, xenotime, rare scheelite and molybdenite, and rheniite also occur as accessory constituents of these carbonate veins.

3.1.2. Skarn Ores

Skarns host the highest grades of Cu and Zn ores within the Recsk ore complex. Skarns occur typically as lenticular or pocket-like bodies with a thickness of 50–200 m, surrounding the mineralized diorite apex. The classification of skarn samples based on mineralogical and textural criteria is more problematic, as the skarn deposits are diverse and several parageneses can be observed even on a hand specimen scale. Skarns at Recsk were classified by their mineralogy as follows [5]: wollastonite marble, garnet–pyroxene skarn, pyroxene (\pm amphibole) skarn, epidote skarn, phlogopite skarn, anhydrite–serpentine skarn, secondary quartzite metamorphosed rocks. All these rock types also bear signs of hydrothermal overprint by a sulfide paragenesis. The following types were identified among the examined samples: garnet–pyroxene skarn with sulfide veins, pyroxene skarn with massive sulfide lenses, pyroxene–amphibole skarn with replacement–vermicular–fabric, and epidote–anhydrite skarn with replacement quartz–anhydrite–sulfide veins, serpentinite with massive sulfide veins, and contact quartzite with grossular with massive sulfide lenses and B-type veins. Any of these rocks may host Fe, Cu, Zn–Pb, or Cu–Zn–Pb mineralization, i.e., the type of mineralization does not seem to depend on contact metamorphic/metasomatic paragenesis.

Most examined samples belong to the garnet skarn. The size of garnet grains varies between 50 μ m and 1 cm. Individual crystals can be euhedral, but they can also be anhedral in veins. Garnet often shows growth-zoning, marked by radially occurring primary 2-phase fluid inclusions. The garnet in these rocks is andradite, less often grossular, showing zonation patterns. As mineral inclusions, diopside, quartz, less often anhydrite, hematite, and sphalerite (Figure 4a) can be found in garnet. The garnet skarns often contain calcite, quartz, pyroxene, epidote–zoisite nodules, tabular anhydrite, and less commonly amphibole, occurring in fibrous clusters.

The pyroxene skarn most often contains massive sulfide ore. Pyroxene has hedenbergite–johannsenite, less often diopside composition, and an average grain size of 200–1000 μ m. Pyroxene shows a isometric–hypidiomorphic habit, but it is idiomorphic and tabular, associated with large (5–10 mm) carbonate grains. It often occurs together with 10–200 μ m crystals of tremolite having a needle-like or fibrous appearance. The pyroxene in the garnet–pyroxene skarn rocks is not significantly different in composition or form from the pyroxene appearing in other skarn rocks. Pyroxene skarn rocks typically contain mostly Cu-rich ore and, less often, Cu–Mo mineralization, appearing as disseminations of chalcopyrite and molybdenite (Figure 4f,g) associated with massive lenses of pyrite.

Epidote–quartz skarn rocks consist of epidote, pyroxene, and anhydrite. These lenses are often crosscut by a network of 1–10 mm-thick veins containing quartz, carbonate, and anhydrite. Epidote is also present in an epidote–chlorite endoskarn; there, the original texture of the diorite and relics of the magmatic mineral assemblage are preserved. In the epidote skarns, the Zn-, Cu–Zn, Zn–Pb sulfide mineralization is typically found in these veins that sometimes comprise up to 10% of the whole rock. Common ore minerals are pyrite, chalcopyrite, and sphalerite. In some samples, scheelite was observed, often accompanied by molybdenite.

Contact metamorphic quartzite occurs along the contact of the diorite intrusion with siliceous rocks. The massive quartzite lenses are often crosscut by thin garnet-bearing calc–silicate veins. Centimeter-sized massive sulfide lenses and B and D quartz–sulfide veins are common in this rock type. They typically contain a pyrite–chalcopyrite–sulfosalt/telluride–tennantite–scheelite paragenesis (Figure 4c,h).

An unusual anhydrous skarn rock of monticellite–magnetite–anhydrite composition was overprinted by a hydrous retrograde mineral association with brucite–hydrogrossular–serpentine–chlorite–tochilinite–valeriite (Figure 4b,d). This is accompanied by pyrite, pyrrhotite, sphalerite, alabandite, and galena, where galena may host Bi–tellurides and sulfosalts as inclusions (Figure 4e).

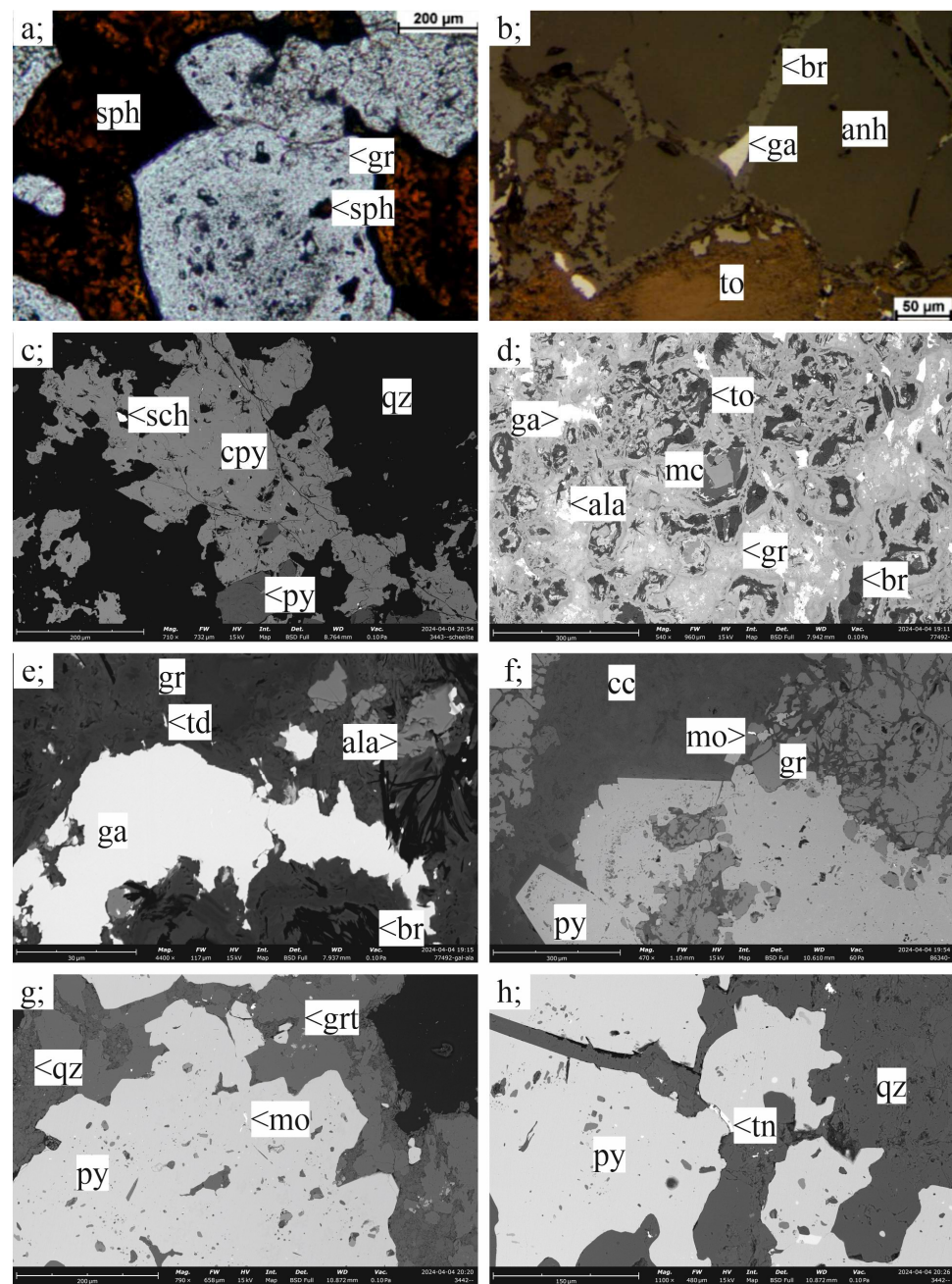


Figure 4. Typical ore textures ((a,b), polarized light), ((c–h), SEM-BSE) from the various skarn mineralized rocks: (a), transmitted polarized light photograph of sphalerite (sph) inclusions in andradite garnet (gr) surrounded by transparent red sphalerite (Rm71–499); (b), reflected polarized light microphotograph of equilibrium-texture anhydrite (anh) being replaced by brucite (br) and galena (ga) along fractures, in pseudomorph equilibrium texture with rust-red tochilinite (to) replacing magnetite (Rm77–492); (c), scheelite (sch) inclusion swarm in quartz–chalcopyrite–pyrite vein in garnet–skarn (Rm34–43); (d), monticellite (mc) being replaced by brucite–tochilinite assemblage surrounded by xenomorphic, vein-filling hydrogrossular (gr), resorbed anhydrite, and hydrothermal galena, pyrite, and alabandite sulfide grains (Rm77–492); (e), Bi-sulfotelluride–tetradymite–(td) grains with anhedral, vein-filling galena associated with sphalerite and alabandite; (f), euhedral pyrite crystals with silicate inclusion zones occurring with grossular and calcite (cc), molybdenite (mo) occurs in a subhedral garnet crystal (Rm45–340); (g), molybdenite inclusions in subhedral, quartz-inclusion-rich pyrite grains in siliceous matrix (Rm34–42); (h), anhedral skarn pyrite with chalcopyrite inclusions crosscut by not zoned tennantite (tn) vein in illite–quartz matrix (Rm34–42).

3.1.3. Carbonate-Replacement Polymetallic Mineralization

Carbonate-replacement (CAR) hydrothermal ores have diverse appearances and occur within variously altered host rocks. This type of mineralization extends as far as 2 km from the porphyry mineralization center. Pyrite-dominated mantos were described as far as 1–1.5 km southwest from the outermost diorite stocks, while few-centimeters-thin carbonate-replacement polymetallic veins occurred up to 2 km from the dioritic bodies in every direction. CAR mineralization is generally represented by altered-recrystallized hydrothermal breccias forming centimeter-sized brecciated veins or a few ten-centimeter-thick breccia pipes in the samples.

The manto ore forms horizontal massive sulfide lenses with a thickness up to few tens of cm. The breccias show a diverse appearance within the mineralized zones. Based on the composition of the clasts, there are exclusively carbonate, carbonate–quartz–clay minerals, as well as exclusively siliceous breccia types, within which the gangue and ore mineral assemblage can show further variability. Among the hydrothermally altered, brecciated sedimentary rocks, the most characteristic common feature is the fragmented and somehow recrystallized bedrock cemented by a carbonate–sulfide \pm quartz \pm anhydrite assemblage. The shape (roundness and sphericity) and size (from a few 10 μ m to >10 cm) of the fragments can vary from sample to sample and within individual samples too. Any rock type within the whole mineralized complex may be cross-cut by carbonate–sulfide \pm quartz \pm sulfate veins of 0.5–5 cm thickness. These veins are characterized by banded texture, the rims being typically enriched in quartz, their central part being most heavily mineralized. Sulfates within these veins may be anhydrite, celestite, or baryte.

The ore mineral content of the rocks varies from sample to sample, usually ranging from below 1% to 5%, although some samples may contain as much as 50% sulfides connected to veins or the matrix. Higher-ore mineral contents were observed locally in sulfide-rich veins with 10–50% of sulfides, dominantly sphalerite–pyrite, while manto-like, horizontally extensive pyritization accompanied by sphalerite, tetrahedrite-group minerals, kesterite, and, rarely, scheelite and molybdenite (Figure 5a,e,g,h) hosts 15–20% ore minerals on average.

Mantos, hydrothermal breccias, and distal altered sedimentary rocks are commonly crosscut by carbonate or carbonate–sulfide veins, often accompanied by quartz and anhydrite. The carbonate vein network enmeshing the whole mineralized system can be characterized by several textural–paragenetic types. There are exclusively carbonate veins without any sulfides present, as well as carbonate–pyrite veins in which pyrite may host inclusions of galena or tetrahedrite-group minerals—rarely kesterite—, and carbonate–sulfide veins with 1–5% pyrite–sphalerite–galena–chalcopyrite–tetrahedrite–sulfosalt ore mineral assemblage. The latter vein generation represents the highest ore grades throughout the entire CAR-mineralized system. Sulfide-bearing veins usually contain various amounts of euhedral quartz and locally also contain sulfates (celestite, anhydrite), sometimes containing fluorite, bastnäsite, xenotime (Figure 5e,h), monazite, apatite, and pockets of clay minerals (usually illite).

Veins containing only various carbonate minerals occur throughout the altered country rocks. Multiple generations of carbonate veins can be distinguished: there are coarse (1–2 mm) crystalline, exclusively calcite-bearing veins which predate the mineralizing carbonate–sulfide veins based on cross-cutting relations. This vein type is usually thin, 1–5 mm in thickness. There are open fissures and cavities filled with carbonate minerals, where calcite is often accompanied by dolomite and minor bastnäsite; even monazite may be present within those veins. The size of calcite crystals in such veins is usually below 1 mm, although, in open cavities, both calcite and dolomite may form rhombohedral crystals with a size up to 5 mm. These veins can reach a thickness up to 2 cm, their outline being sharp. Both mineralogical and cross-cutting relations suggest that these veins were formed during the post-ore stage. Although sulfides are absent in these carbonate veins, they usually occur in samples with disseminated ore types. There are pure calcite, pure dolomite, or calcite–

dolomite veins, all crosscutting every preexisting mineralized feature. These are usually fine crystalline (below 0.5 mm), and their thickness is usually also maximally 1–2 mm.

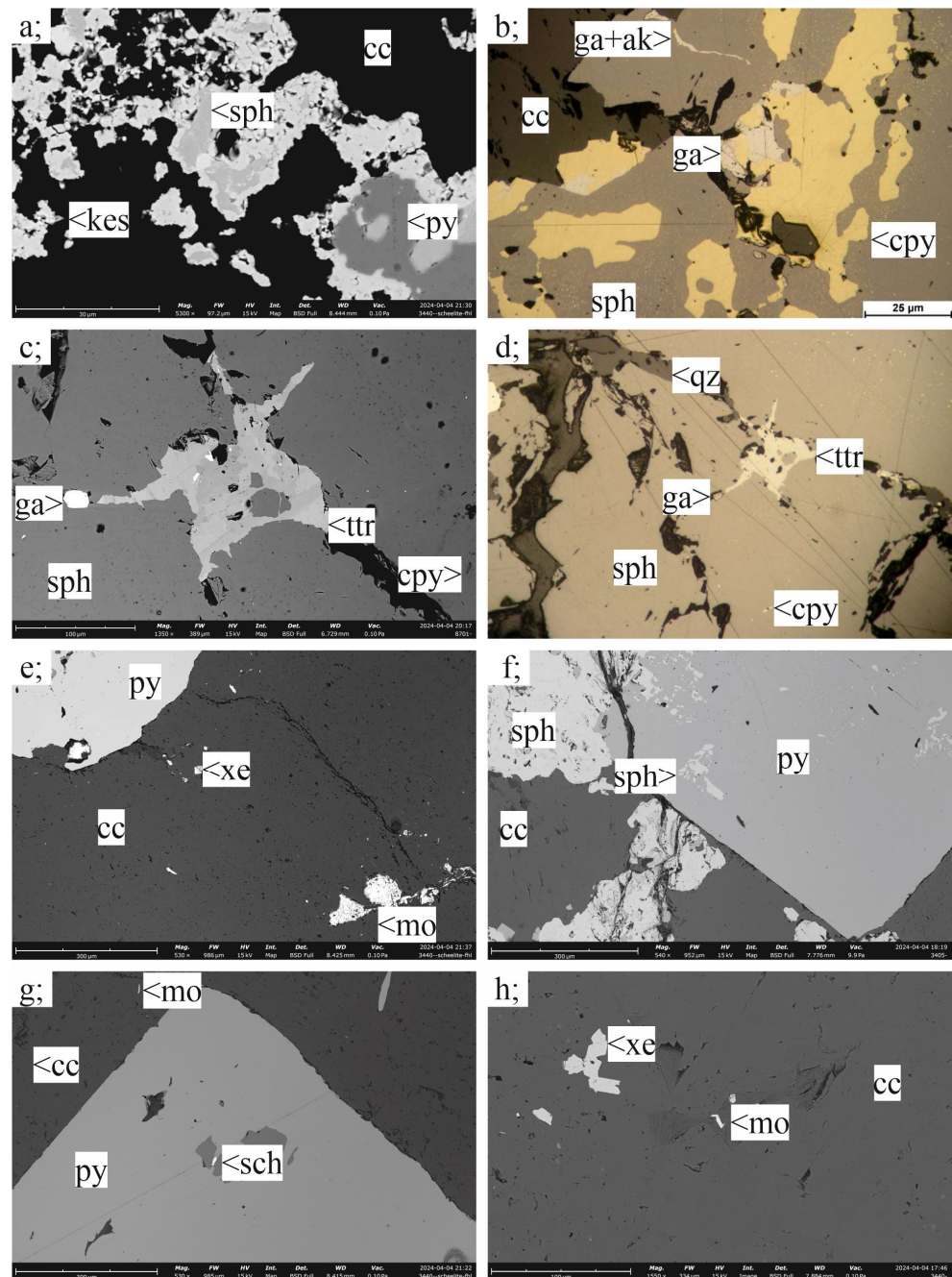


Figure 5. SEM-BSE (a,c,e–h) and reflected-light (b,d) microphotographs of characteristic ore textural features from the CAR mineralization type: (a), kesterite–kuramite (kes) rim on resorbed sphalerite (sph) and pyrite (py), accompanied by tetrahedrite, sphalerite showing network-like and granular kesterite disease (Rm34–07); (b), chalcopyrite (cpy) replacing both sphalerite and galena (ga) with characteristic dusted disease in sphalerite associated with aikinite (ak) domains replacing galena in vein (Rm61–01); (c,d), oscillatory zoned tetrahedrite (ttr) patch in sphalerite associated with galena and the same grain in reflected polarized light (Rm87–01); (e), microcrystalline molybdenite (mo) patches in massive carbonate (cc) manto with pyrite (Rm34–07); (f), unaltered sphalerite (sph) with poikilitic texture in euhedral pyrite surrounded by subhedral sphalerite (sph) grains showing dusty chalcopyrite disease (Rm34–05); (g), scheelite inclusion in euhedral pyrite (Rm34–07); (h), molybdenite flakes within illite-bearing vein in carbonate manto associated with idiomorphic xenotime (Rm34–07).

Carbonate–pyrite veins are typical both for mantos, and for country rocks crosscut by massive carbonate–Zn–Pb sulfide veins. There are veins hardly reaching a thickness of 1 mm, with pyrite and calcite being present within them, while other carbonate–pyrite veins can reach a thickness of 1 cm or more. Pyrite within these veins is typically euhedral, accompanied by calcite and dolomite mostly. Accessory minerals in these veins can be bastnäsite, and various minor sulfides found as inclusions in pyrite, such as sulfosalts, sphalerite, galena, and kesterite. In their thickness and their mineral composition, they can be distinguished from veins having more various sulfide mineralogy.

Carbonate–sulfide veins are one order of magnitude thicker within the samples than the previously mentioned groups. Their carbonate mineralogy is dominated by Mn-bearing calcite, dolomite, ankerite, and, rarely, siderite. Drusy quartz with sulfide inclusions is also a common constituent of these veins. Both the pyrite–sphalerite–galena–tetrahedrite–group minerals dominated ore mineral composition, and the various carbonate phases may occur with various crystal sizes between 1 mm and 3 cm. Carbonate–sulfide veins are generally the thickest, reaching thicknesses over 12 cm within the samples, although they are often interlocking and braided. Thus, a 1–4 cm vein is often accompanied by 1–5 mm sized nearly parallel-running veins with similar mineralogy.

Some quartz–carbonate–sulfide veins with accessory anhydrite, celestite, barite within the porphyry apex share the textural, mineralogical, and paragenetic sequential properties of the veins occurring within the carbonate-replacement zones.

3.2. Ore Mineralogy

3.2.1. Porphyry Mineralization

Pyrite is the dominant mineral in the disseminated ore, with various sizes and shapes ranging from 10 μm euhedral to 1 cm subhedral–euhedral crystals. In addition to pyrite, chalcopyrite and molybdenite are locally abundant (Figure 3), primarily as inclusions in pyrite, less often as an independent phase. Pyrrhotite, bornite, sphalerite, galena, tennantite, and various sulfosalts may also occur (Figure 6). Chalcopyrite is never euhedral; it occurs as anhedral 20 μm to 1 cm patches, surrounding pyrite, or as individual sulfide veinlets (Figure 3c–e). Disseminated molybdenite occurring in the diorite is typically 20–50 μm in size, with thin flakes mostly embedded in clay or quartz, replacing primary porphyry components. Disseminated pyrite replaces altered-porphyry grains of any size from 200 μm to 2 cm. The edge and outline of the altered magmatic phenocryst is often contoured by anhedral sulfide mineral nodules (Figure 3a), or the ratio of sulfide replacement increases towards the tips of the porphyritic phenocryst. Zonal sulfide replacement is also common, where the distribution of the fine-grained, typically anhedral–subhedral pyrite and chalcopyrite grains follow the growth zones of the porphyry crystals. Sulfides replacing the phenocrysts are often found alongside dominantly idiomorphic apatite grains zoned with xenotime or monazite inclusions. In the altered matrix of the diorite, which is typically silicified with clay minerals, the enrichment of the sulfides can be associated with a thin, μm -scale crack system that can only be recognized under the microscope. The cracks contain predominantly quartz, pyrite and chalcopyrite. Rarely, disseminated idiomorphic pyrite, molybdenite, or sphalerite grains appear, which cannot be connected to any visible vein or to the position of a previous mineral phase in the matrix. Pyrite with inclusions of galena, sulfosalts, and chalcopyrite, sometimes with inclusions of bornite and kesterite, was the first phase to crystallize. Pyrite rims are often co-crystallized with idiomorphic molybdenite flakes. Chalcopyrite generally occurs as space-filling xenomorphic replacive masses in the porphyry phenocrysts, or as late-stage veins cross-cutting the earlier assemblages. The extent of these latter veins is often limited to the replaced phenocrysts. Aluminum–phosphate–sulfate minerals, apatite, monazite, and hydrothermal zircon of 30 μm size may appear in nests of clay minerals besides the sulfides.

often accompanied by pyrite and chalcopyrite in B-type veins; pyroxene–garnet skarns host dispersed 0.1–5 mm subhedral pyrite grains within the silicate matrix; while idiomorphic pyrite crystals of 0.1–2 mm size may occur as dispersed crystals, rarely as vermicular veins in pyroxene or pyroxene–amphibole–skarns.

Chalcopyrite generally forms xenomorphic masses within all skarn rock types (Figure 4c). Massive quartz–chalcopyrite lenses occur in pyroxene skarn samples with 10–30% chalcopyrite locally, chalcopyrite with xenomorphic sugary quartz occurring in an 100–1000 µm wide vein network enmeshing the whole pyroxene skarn. Chalcopyrite in these samples locally shows alteration to covellite along the grain boundaries. In Zn–skarn samples chalcopyrite occurs mostly as chalcopyrite disease in sphalerite, often replacing as much as 15% of the original sphalerite grains. Euhedral–subhedral sphalerite and galena tend to occur together. Early sphalerite shows co-precipitation textures with andradite (Figure 4a), while sphalerite is also observed to co-precipitate with pyrite and galena. Sphalerite grains in Zn–Pb skarns are typically 0.1–2 mm in size, occurring in bands typically accompanied by subhedral–euhedral 0.1–5 mm galena and euhedral 0.1–2 mm pyrite. Further ore minerals are of less importance. Alabandite (Figure 4d,e) occurs usually in subhedral 20–200 µm grains, often accompanied by high-Mn high-Fe sphalerite and space-filling galena. Valeriite and tochilinite were only observed in one of the studied samples, accompanied by brucite, serpentine-group minerals and hydrogrossular, replacing magnetite, monticellite, and anhydrite (Figure 4d). Tochilinite and valleriite within this skarn assemblage are often intergrown, forming xenomorphic masses with 20–600 µm pseudomorphs after the pre-existing equilibrium-textured magnetite–monticellite assemblage (Figure 4b). In the original silicate–oxide mineral assemblage of the skarn, hematite and magnetite can be observed as ore minerals and as accessories, as well as accessory allanite, thorianite, rutile, and perovskite. Sphalerite in most of the studied skarn samples shows intense “chalcopyrite disease”.

3.2.3. Carbonate-Replacement Mineralization

The most abundant ore mineral throughout the mineralized carbonate host rocks is pyrite with varying size and shape depending on textural position, commonly associated with sphalerite-, galena-, chalcopyrite-, and tetrahedrite-group minerals (Figure 5a,e–g; Figure 6). In addition, accessory molybdenite, scheelite, kesterite, kuramite, aikinite, friedrichite, bismuthinite, telluro-, cupro-, or plumbobismuthinite, tetradymite, hessite, and emplectite occur in the mineralized samples (Figure 6). While molybdenite and scheelite occur as <1% separate phases, kesterite usually occurs connected to sphalerite- or tetrahedrite-group minerals, while the sulfosalts are generally present as 5–20 µm inclusions within pyrite or galena. The ore minerals can either occur in the breccia clasts or in the cementing carbonate vein network.

Pyrite occurs exclusively as 10–500 µm large cubes in the silicified host rock and 100 µm–4 mm large crystals in carbonate veins. Pyrite is generally the first phase to crystallize, often showing growth zonation bands. Inclusions of sphalerite-, galena-, tetrahedrite-group minerals, chalcopyrite, and, rarely, arsenopyrite highlight the zonal patterns visible in pyrite. Pyrite has a typical poikilitic [44] co-precipitation texture with sphalerite occurring in some CAR-mineralized veins (Figure 5f). Sphalerite also occurs as euhedral–subhedral grains, with typically amber, rarely bluish-yellow, or dark-brown color. Early precipitating sphalerite may occur as zonal inclusion swarms in pyrite or euhedral quartz, while sphalerite in carbonate veins is usually intergrown with pyrite and galena, showing polysynthetic twinning. Multiple growth zones of sphalerite can be observed, typically being highlighted by color changes. All samples with sphalerite are characterized by the intense “chalcopyrite disease” (Figure 5b,d) [45]. Chalcopyrite displaces up to 10–15% of the original crystal generally, although the extent of the disease can be different in every specimen. Besides chalcopyrite, kesterite occurring together with tetrahedrite also replace sphalerite (Figure 5a). Sphalerite grain size ranges from 5 µm to 3 cm within different textural positions.

Galena usually is co-genetic with sphalerite, although some galena veins also cut across sphalerite crystals, suggesting a later origin. Galena is typically subhedral, always occurring in the same textural position as sphalerite both in the matrix or in the carbonate veins. The typical crystal size for galena is between 50 μm and 3 mm. In some sphalerite-bearing specimens with chalcopyrite disease in sphalerite, galena shows cellular–granular, amoeboid, or less commonly, oriented lamellar replacement texture by aikinite [46] as a quasi “galena disease”.

Besides its typical occurrence as “disease in sphalerite”, chalcopyrite generally occurs as veins or anhedral patches of 50 μm –10 mm size. Chalcopyrite veining typically shows crosscutting relations with every ore mineral except the late-stage tetrahedrite-group minerals. The tetrahedrite-group minerals occur as 100–500 μm space-filling anhedral masses, veins, or pockets often accompanied by anhedral galena or rarely with hessite and bismuthinite. Kesterite only occurs as rims on diseased sphalerite crystals often accompanied by vanadium-rich sulvanite and tin-rich kuramite-like mineral phases.

3.3. Compositions of Major Sulfide Minerals in Different Types of Mineralization

Galena, sphalerite, tetrahedrite-group minerals, molybdenite, and bismuth-bearing sulfosalts all occur in porphyry, skarn, and carbonate-replacement type of ores at Reesk. Thus, comparison of their compositions may indicate their different formation conditions in different parts of the porphyry-, skarn-, and carbonate-replacement-ore-forming system at subvolcanic levels. Chemical compositional data are given in the electronic supplement.

3.3.1. Molybdenite

In molybdenite, the concentrations of Cu, Se, Re, and W are highly variable. Rhenium is the most abundant trace element with a wide range of concentrations. Molybdenite in the porphyry copper ore shows the highest Re contents up to 4.47 wt% ($\bar{x} = 1.05$ wt% and $2\sigma = 1.22$, $n = 47$). Molybdenite with the highest Re contents was found in the northernmost apexes of the diorite intrusion where molybdenite is often hosted by D-type quartz veins and carbonate veins with pyrite–molybdenite–galena occurring in the central part of D-type veins. Molybdenite grains within these veins also tend to show heterogeneous distribution of Re. Rhenium contents show no systematic changes throughout most of the grains but oscillatory zoning and lamellar changes in the distribution of Re occasionally also occur. In those latter cases, Re contents tend to change by various layers within one single molybdenite flake. Molybdenite grains with the highest Re contents also host micrometer–nanometer-sized inclusions of rheniite. Molybdenite in the skarn and CAR mineralization shows significantly lower rhenium concentrations compared to the porphyry ore (Figure 6). The Re content of molybdenite is 0.026–1.86 wt% with $\bar{x} = 0.267$ and $2\sigma = 0.359$ ($n = 30$) in the skarn ores, and it is always below 0.125 wt% with $\bar{x} = 0.047$ wt% with $2\sigma = 0.039$ ($n = 13$) in the CAR mineralization.

The Cu contents of molybdenite show a reverse trend compared to Re. The distal CAR mineralization has the highest Cu contents, while lower values characterize both the skarn and porphyry ores (Figure 7a). In the two latter mineralization types, the Cu values are mostly below the detection limit, while they are always detectable in the CAR mineralization. The Se concentrations in molybdenite show a similar trend as Cu (Figure 7). Selenium is generally low in molybdenite from both the porphyry (b.d.l–0.14 wt% $\bar{x} = 0.024$ wt% with $2\sigma = 0.027$, $n = 47$) and skarn (b.d.l–0.034 wt% $\bar{x} = 0.01$ wt% with $2\sigma = 0.011$, $n = 30$) ores, though some molybdenite from the porphyry ore have sporadically higher values. The average Se content in molybdenite is highest in the CAR mineralization (up to 0.11 wt% $\bar{x} = 0.06$ wt% with $2\sigma = 0.030$, $n = 13$). Tungsten does not show systematic variation among the three mineralization types, but only a few values ($n = 12$ out of 90) are above the detection limit (180–200 ppm) of the applied analytical setup. These higher values were measured dominantly in molybdenite from the skarn mineralization.

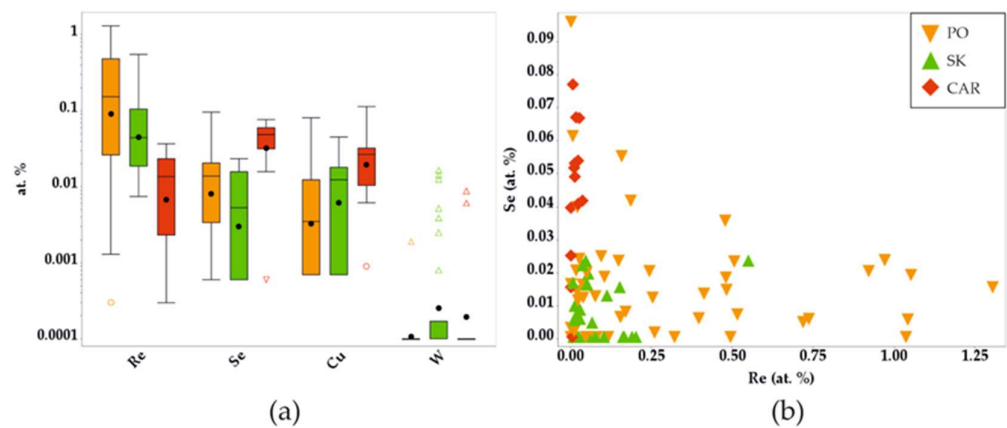


Figure 7. Minor and trace element distributions in molybdenite from the three mineralization types (Porphyry (PO), skarn (SK), and carbonate-replacement (CAR)). (a) Boxplots showing the trace element distributions and their interquartile ranges, averages (horizontal lines within the boxes), and medians (black circles) for the three mineralization types. Note that the y -axis is logarithmic. While Re shows a decreasing trend from the porphyry towards the carbonate rocks, Cu and Se are both seemingly enriched towards the more distal mineralization. (b) Re–Se (atom%) scatterplot showing generally low Se contents coupled with high Re in porphyry, while low Re with relatively higher Se contents in the carbonate-replacement mineralization.

When plotting Re vs. Se data of molybdenite, a grouping of the data according to the mineralization type becomes visible (Figure 7b). The Re contents of molybdenite are lower in the skarn and especially in the CAR mineralization types reaching the highest values in the porphyry molybdenite. In contrast, Se contents are highest in molybdenite from CAR mineralization. Molybdenite with high Se and low Re contents usually is from carbonate veins hosting only pyrite besides molybdenite. Skarn molybdenite has low concentrations of both Se and Re and overlaps with the lower range of porphyry mineralization (Figure 7b).

3.3.2. Galena

Galena is a common ore mineral in all three mineralization types at subvolcanic levels at Recksk. It shows variations in Se, Ag, and Bi contents according to the ore type (Figure 8a,b). Selenium is lower in the porphyry copper ore (b.d.l.–1.54 wt%, \bar{x} = 0.53 wt% and 2σ = 0.1, n = 39) compared to the skarn (0.23–2.13 wt%, \bar{x} = 0.97 wt% and 2σ = 0.51, n = 45), and peripheral CAR mineralization (0.35–4.08 wt%, \bar{x} = 1.01 wt% and 2σ = 0.95, n = 34) (Figure 8a). Silver and Bi show a strong positive correlation (Figure 8b) with r = 0.94 for the whole set of samples. The highest Ag and Bi contents are both found in the CAR type. Galena analyses with Ag values above the detection limit show a negative correlation of Se and Ag (r = 0.72). Porphyry mineralization hosts galena with Ag (b.d.l.–0.76 wt%, \bar{x} = 0.11 wt% and 2σ = 0.19, n = 39) and Bi (b.d.l.–0.75 wt%, \bar{x} = 0.06 wt% and 2σ = 0.16, n = 39) contents, and galena from the skarn mineralization shows similar range of Ag (b.d.l.–0.43 wt%, \bar{x} = 0.10 wt% and 2σ = 0.14, n = 45) and Bi (b.d.l.–0.28 wt%, \bar{x} = 0.05 wt% and 2σ = 0.09, n = 45) contents. Galena in the CAR mineralization contains the highest amount of both Ag (0.18–0.97 wt%, \bar{x} = 0.50 wt% and 2σ = 0.24, n = 34) and Bi (b.d.l.–1.28 wt%, \bar{x} = 0.43 wt% and 2σ = 0.4, n = 34, respectively). Copper was also analyzed in galena, showing the highest values in the porphyry mineralization, although the data may be affected by chalcopyrite hosting most of the measured galena grains. Thus, Cu data are not further used for deposit type characterization.

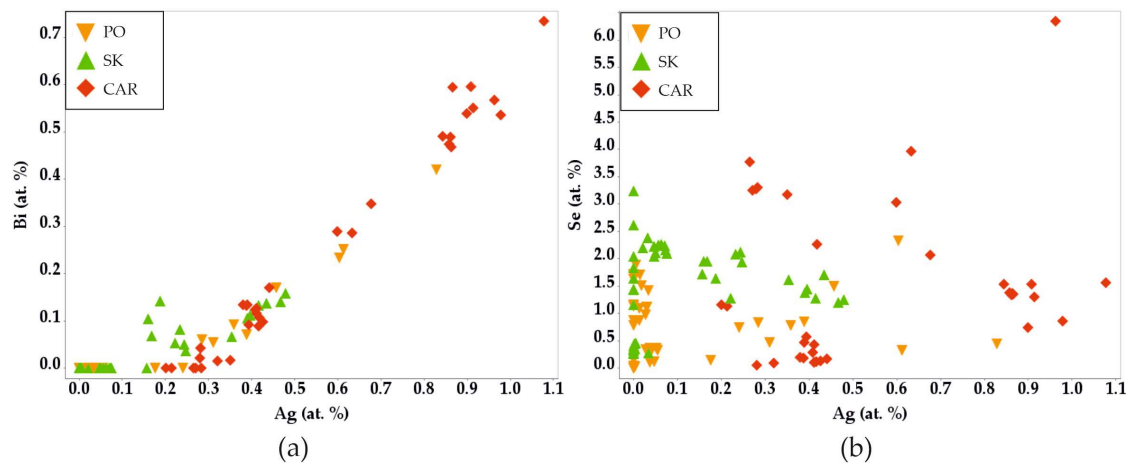


Figure 8. (a): Ag–Bi (atom%) scatterplot for galena. Linear correlation is visible, with increased Ag–Bi contents characteristic to CAR mineralization, while skarn mineralization shows similar trends to porphyry. (b): Ag–Se scatterplot for galena shows the lack of correlation between these elements.

For the whole galena dataset above detection limit for Bi ($n = 51$), the following linear regression can be set for Ag–Bi compositions with a correlation ($r = 0.92$):

$$\text{Bi(at. \%)} = 0.7512\text{Ag(at. \%)} - 0.1634 \quad (1)$$

If skarn data are excluded—as it shows a different behavior regarding Ag–Se—the remaining porphyry–carbonate–replacement dataset shows a correlation of ($r = 0.97$) for Bi and Ag. With this dataset ($n = 37$), the linear regression can be modified as follows:

$$\text{Bi(at. \%)} = 0.8387\text{Ag(at. \%)} - 0.2243 \quad (2)$$

3.3.3. Sphalerite

Sphalerite is characterized by variable Fe, Mn, Cd, and V contents while Cu occurs in sphalerite mostly due to intense “chalcopyrite disease” (Figure 5b) [45]. Thus, high Cu contents are also often associated with similarly high Fe contents, although higher Fe contents are generally observed with Cu being totally absent. All the analyzed sphalerite crystals are generally low (below detection limit) in Ge, In, and Hg. Some exceptions of relatively higher In contents (0.58–0.69 wt%, $n = 3$) coincide with enrichments of Cu, with no other elements being significantly enriched. All of the above-mentioned In enrichments occur in one CAR sample, showing extensive chalcopyrite disease in all sphalerite grains. Principal component analysis (PCA) of the data (Figure 9.) shows Mn and Fe charging positively on PC2 while being negatively loaded on PC1. Cadmium and Zn show an inverse behavior compared to Fe and Mn, although their characteristics are less distinctly highlighted. Loading positively on both PC1 and PC2, Cu shows a nearly perpendicular trend to all of the aforementioned elements. Hence, while high Mn contents are typical for skarn sphalerite, porphyry sphalerite is Zn–Cd-dominated, while CAR mineralization tends to fall in between, overlapping with the skarn data field.

3.3.4. Kesterite

Besides the chalcopyrite disease, kesterite $\text{Cu}_2(\text{Zn,Fe})(\text{V,In,Sn})\text{S}_4$ is also found replacing sphalerite with a similar texture (Figure 5a) in the CAR mineralization. Sulfides with $\text{Cu}(\text{Zn, Fe})(\text{Sn,V})(\text{S,Se})$ element association occur as inclusions in pyrite together with sphalerite, chalcopyrite, and bornite within the porphyry orebody too. Multiple generations of kesterite have been found as inclusions of pyrite, replacing sphalerite in the CAR mineralization or accompanying tetrahedrite-group minerals (Figure 6), some of them containing significant amounts of V (up to 3.22 wt%, $\bar{x} = 0.66$ wt% $n = 18$), and sometimes remarkable amounts of In too (up to 0.63 wt%, $\bar{x} = 0.25$ wt% $n = 18$). Both in the porphyry and the

CAR mineralization, crystals of ferrokesterite–stannite occur. Moreover, composition close to kuramite is detected, although within these grains, Fe, Zn, In, and V substitutions also occur, which are known as substitutions within this structure.

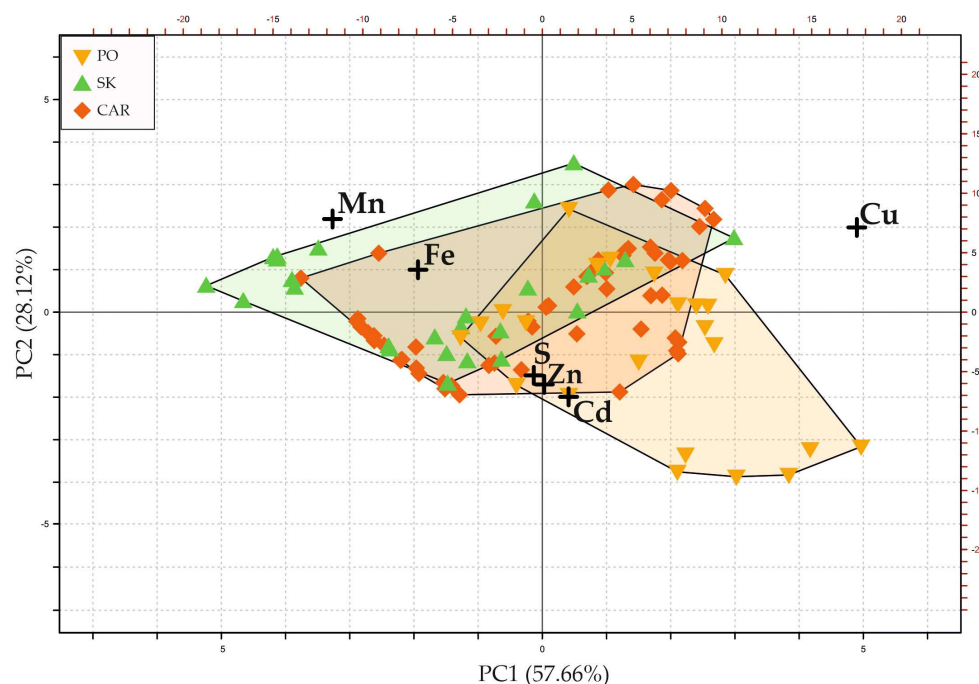


Figure 9. PCA biplot of sphalerite main element compositions from the studied mineralization types. Vector endpoints are indicated by black crosses. Iron and Mn showing inverse behavior compared to Zn and Cd is a result of the well-known substitution mechanisms for these elements, while Cu loading nearly perpendicular to these is an effect of abundant chalcopyrite disease within the sphalerite grains. While porphyry sphalerite can be characterized by relatively higher Cd and Zn contents, skarns are marked by elevated Mn levels. CAR field is falling in between, overlapping strongly with the majority of the skarn data.

3.3.5. Tetrahedrite-Group Minerals

Major and minor element compositions for tetrahedrite-group minerals were also measured from all three deep-seated mineralization types, while data for the epithermal mineralization are available from [13]. It is important to highlight that skarn data come from one single sample, as occurrence of tetrahedrite-group minerals within the skarn mineralization is rather accidental. While the CAR-mineralized zones are dominated by the presence of tetrahedrite, tennantite is dominant in the porphyry and the skarn samples.

Tetrahedrite group minerals in all three mineralization types show strong ($r = 0.72$) correlation between Sb and Ag, while its Fe and Cd contents are negatively correlated ($r = 0.70$). Oscillatory zoning is often observed in the CAR mineralization (Figure 5c), where multiple zones within one single grain were also measured. Due to oscillatory zoning patterns, tetrahedrite- and tennantite-rich compositions may occur next to each other on the single-grain-scale in the CAR mineralization. On the contrary, tennantite is predominant in the porphyry and skarn mineralization; in the latter, zoning is lacking. Oscillatory zoning is caused by changes in As, Sb, Ag, Fe, Zn, and Bi contents, As–Sb being the most influential substitution. While CAR mineralization is characterized by oscillatory zoned tetrahedrite, the mineral grains in the porphyry mineralization are generally homogeneous or can be characterized by one single Sb-enriched rim.

Mineralization types within the porphyry–epithermal system can be distinguished by the $\text{Ag} + \text{Cu}/\text{Fe} + \text{Zn}$ (apfu) ratios [13] or $\text{Sb}/(\text{Sb} + \text{As})$ (apfu) ratios, as well as $\text{Fe}/(\text{Fe} + \text{Zn})$ (apfu) ratios [27] in the tetrahedrite-group minerals (Figure 10.). Porphyry samples show $\text{Sb}/(\text{Sb} + \text{As})$ ratios of 0.00014–0.46, i.e., these are tennantite. $\text{Sb}/(\text{Sb} + \text{As})$ ratios between

0.9 and 0.007 are characteristic for the CAR mineralization type. As mentioned, the wide range of this ratio is caused by oscillatory zoning of this mineral. A single generation of tennantite grains ($n = 14$) found in a sample from skarn mineralization is characterized by $Sb/(Sb + As)$ values of 0.0008–0.026.

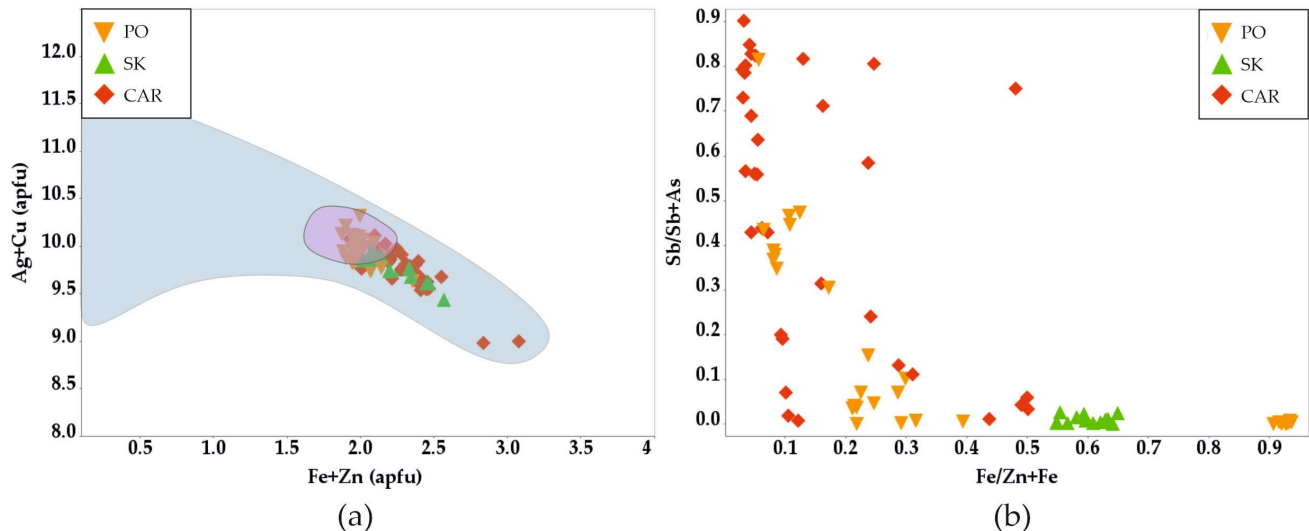


Figure 10. (a): Ag + Cu – Fe + Zn scatterplot of tetrahedrite-group minerals showing the data of the deep-seated mineralization types (this study) compared to data fields of all three generations of epithermal high-sulfidation (blue) and intermediate-sulfidation from the Parád area (pink) from [13]. (b): Sb/(Sb + As) – Fe/(Fe + Zn) scatterplot of tetrahedrite-group minerals showing the deep-seated mineralization types. Relatively lower Fe contents are characteristic for the CAR mineralization, while relatively higher As contents are characteristic for the porphyry and skarn mineralization types.

Elevated Ag values in the tetrahedrite-group minerals are characteristic for the CAR mineralization type, together with the elevated contents of Sb. Antimony and Bi also show elevated concentration in the CAR mineralization type, although no correlation of Bi with Sb or Ag was found. Fe/(Fe + Zn) in tetrahedrite-group minerals is less distinctive because this ratio shows bimodal distribution in the studied samples, with values between 0.94 and 0.90, as well as 0.40–0.06 for Cu–porphyry. In the skarn, Fe/(Fe + Zn) is 0.64–0.54, and CAR mineralization is richer in Zn (0.50–0.03). Cadmium, occurring in the same crystallographic position as Zn, shows enrichment in the porphyry mineralization, while being constantly lower in the CAR mineralization.

3.3.6. Bismuth Sulfosalts

Bismuth sulfosalts are typical accessory minerals in all ore types at Rečsk. The sulfosalts from high-sulfidation and intermediate-sulfidation epithermal mineralization were already described in detail before [8,13], but less so in the deep-seated orebodies addressed in this study. Bismuthinite, galenobismuthinite, and tetradyomite occur in all the mineralization types in various amounts. Copper–Pb–Bi ratios allow distinction of different mineral species (Figure 11), such as aikinite–bismuthinite series minerals as well as friedrichite, cosalite, cuproillianite, wittichenite, and cuprobismuthinite homologous series.

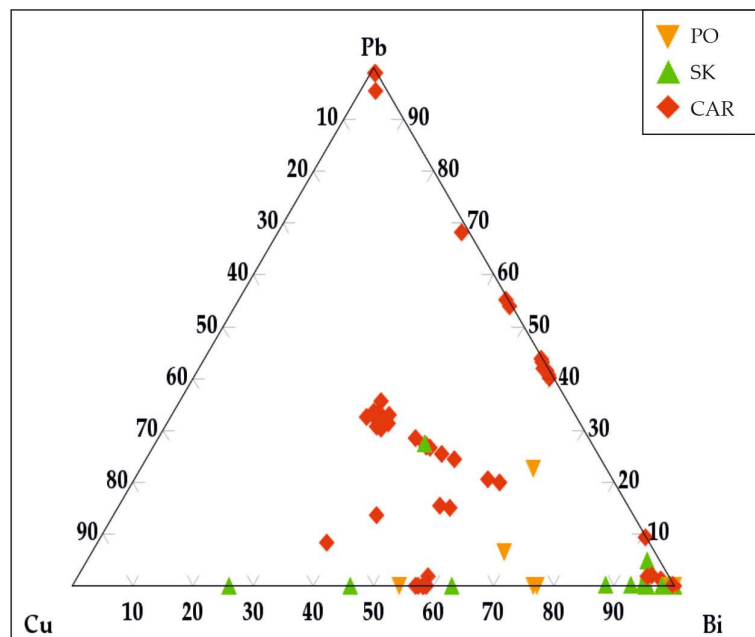


Figure 11. Pb–Cu–Bi ternary plot of the measured Bi sulfosalts. Most sulfosalts grains were found within the CAR mineralization type, most of them being typically Pb-rich, while Pb-bearing sulfosalts phases are less abundant in skarn and porphyry mineralization. PO mineralization is dominated by Cu-bearing sulfosalts, while skarn rocks typically host Pb-poor sulfosalts phases. CAR mineralization hosts a variety of sulfosalts along the aikinite–bismuthinite homologous series and plumbobismuthinite is also abundant.

Identified Ag-bearing Bi sulfosalts are matildite, dantopaite, and hammarite, while an unknown Ag–Bi–Se–S phase could not have been better identified because of its small crystal size. EDS and EPMA measurements for this unknown phase suggest a 3:2 ratio member of the bohdanowitzite–matildite series. Tellurium-bearing phases are similarly abundant in all ore types, and the abundance of Te–Se–S phases show no difference among ore types.

The amounts of identified Bi minerals show some correlation with the type of ore, e.g., aikinite and galenobismuthinite often replace galena in CAR mineralization, while the skarn mineralization is dominated by Pb-poor sulfosalts, like bismuthinite–cuprobismuthinite or tetradymite, and Ag-bearing sulfosalts are also more abundant. Lead-bearing sulfosalts phases are more abundant in the CAR-mineralization type, though emplectite, aikinite–bismuthinite, wittichenite, and hessite occur as accessories within the epithermal, as well as the deep-seated, orebodies.

4. Discussion

Petrography, supported by mineral minor and trace element measurements can serve as a useful tool for mineral exploration in porphyry and related ore deposits. For this purpose, galena, molybdenite, sphalerite, tetrahedrite-group minerals, and sulfosalts can also be discussed regarding stoichiometric, non-stoichiometric, and coupled substitutions documented in the studied mineralization types [16,24,25,27,47–52].

4.1. Molybdenite

In molybdenite, the most notable difference is the change in Re content in the three deep-seated mineralization types (Figure 7). Rhenium gradually decreases from the porphyry mineralization center towards the more distal CAR mineralization, while other elements such as Cu, Se, or W show less distinct characteristics. Detection frequency and quantity of Cu increased from the porphyry stocks towards the distal CAR ore in the carbonate rock. Measurable contents of W were most often analyzed in molybdenite from

skarn rocks, which are typically characterized by a low Re content. Higher W contents coincide with occurrences of scheelite within the skarn. It should be emphasized that molybdenite characterized by the highest Re content occurs in carbonate–quartz–sulfide veins of the porphyry mineralization. Moreover, these Re contents are seemingly decreasing with increasing distance from the porphyry mineralization center as already described by Terada et al. [26]. This agrees with the observations of Barton et al. [24], who found high Re content in less felsic diorite intrusions, where the main controls of its precipitation are more oxidative conditions or phase separation. As anhydrite is documented in the porphyry mineralization, relatively oxidized conditions are a realistic assumption for the Reesk porphyry system, while phase separation is also known to occur in the apexes of the mineralization [10,37], where the D-type and carbonate veins are both abundant. The fact that W and Cu occur in molybdenite within mineralization types lacking rhenium also agrees with observations by Barton et al. [24]. These findings altogether indicate that the main source of Re are the subvolcanic or deeper intrusions, and Re can be preferentially enriched in the open fissures of shallow stockwork mineralization simultaneously with the opening up of late veins. Molybdenite from these veins has the highest Re contents (up to 4.47 wt%), and it is associated with rheniite, a rare rhenium mineral.

4.2. Galena

The strong positive correlation of Ag and Bi in galena (Figure 8.) clearly supports the well-established coupled substitution mechanism along the galena–lillianite series [49]. The second significant trace element substituting in galena is Se, which enables continuous S–Se substitution along the galena–clausthalite line [47]. The variable but typically low Cu contents measured in galena raise the possibility of $\text{Cu}^+ + \text{Bi}^{3+}$ -coupled substitution: $x(\text{Cu}^+ + \text{Ag}^+) - x\text{Bi}^{3+}$ [47,49]. The difference between $\text{Cu}^+ - \text{Bi}^{3+}$ and $\text{Ag}^+ - \text{Bi}^{3+}$ replacement can be that galena–matildite or galena–lillianite form a nominally continuous series [47,49,53], while aikinite and galena are not known to form an isomorphous series. The aikinite that developed as lamellar or myrmecitic replacement phase in Ag–Bi bearing low Cu galena in CAR mineralization further supports the hypothesis that Cu is less compatible with the crystal structure of galena. The established linear functions for Ag and Bi substitution suggest that for one atom % Ag, approximately 0.6 atom % Bi is incorporated. This means that Sb or As—not measured within this study—may also be incorporated within the galena lattice via coupled substitution, or that other substitutions must be operative [51]. The negative correlation of Ag and Se in skarn galena for values above the lower detection limit for Ag suggests that this galena generation has distinctly different formation conditions, which could reflect the metasomatic processes associated with multi-stage skarn formation.

Galena in porphyry copper and skarn systems is generally characterized by lower Se, Ag, and Bi concentrations compared to the carbonate replacement mineralization. Although the enrichment of all three elements towards the country rocks seems statistically valid, Se shows no correlation with Ag or Bi; thus, its enrichment towards the country rocks is not controlled by the same process causing the enrichment in Bi and Ag. Temperature-dependent changes in galena chemistry are suggested by Craig [53] and Moëlo et al. [49]. The observed patterns in this study underline distance-dependent enrichment processes for Se or Ag and Bi in galena which although Se and Bi–Ag have different enrichment processes. Thus, besides temperature, additional factors must be considered, regarding the enrichment of various elements in galena. Partitioning between sphalerite and galena or further co-existing sulfides like pyrite or chalcopyrite may be present regarding some of the elements.

4.3. Sphalerite

Sphalerite minor and trace element distribution can be affected by the source of the elements and the changes in redox conditions in addition to the changes in temperature [23]. Given that the Ga content of high-temperature hydrothermal sphalerite usually falls below the detection limit of the EPMA method, and Ge as well as In are b.d.l. for more than

70% of the measurements, the sphalerite GGIMF thermobarometer of Frenzel et al. [23] is not applicable for our dataset. Both Fe and Mn occur in very low concentrations in sphalerite from the porphyry copper ore, and both elements show high values in the typically more reduced skarn rocks. In the skarns, this may indicate the subsequent hydrothermal overprinting of the previously formed, high-temperature mineral association [54]. Thus, we suggest that the highest Fe–Mn content measured in sphalerite formed in association with tochilinite, valleriite, alabandite, chalcopyrite, galena, and pyrrhotite during the hydrothermal overprinting/metasomatic replacement of the primary high-temperature magnetite–monticellite skarn mineral assemblage. PCA of sphalerite major element data supports that Fe and Mn behave geochemically similarly, following the well-known Mn and Fe substitution of Zn in sphalerite Frenzel et al. [23]. Cadmium shows opposite behavior to Fe and Mn, which can be interpreted with simple substitution processes. Copper loading nearly perpendicular to the Zn–Cd–Fe–Mn line on the PCA figure (Figure 9) indicates that the enrichment of Cu within sphalerite is caused by an independent process. The interpretation of elevated Cu contents is rather easy in most of the studied sphalerite grains as the whole mineralization is characterized by intense chalcopyrite disease in sphalerite [45]. The appearance of In, V, and Ge is not systematic, although their enrichment is usually associated with some subsequent hydrothermal overprinting of sphalerite. Thus, highest In, V, and Ge contents are associated with chalcopyrite or kesterite “disease”, typically in the skarn and carbonate replacement mineralization types. Application of further thermobarometers [22,55] is also limited because of the occurrence of extensive chalcopyrite disease re-equilibrating the Fe content of sphalerite, while Mn and Cd were not measured from galena. To apply modern geothermometers on these sphalerite grains sulfur isotopic ratios of sphalerite and pyrite, fluid inclusion studies, and further trace element analysis must be performed.

4.4. Tetrahedrite-Group Minerals

For tetrahedrite-group minerals, both compositional and textural differences are discriminative. As tetrahedrite-group minerals in skarns are rather rare, the data presented are statistically not representative, as all results originate from one single sample. Tetrahedrite group minerals from the solely examined skarn sample are similarly rich in As as the porphyry mineralization is. They are enriched in Bi, while the concentrations of Se, Ag, and Cd are generally low, below the detection limit. Carbonate-replacement mineralization is dominantly characterized by tetrahedrite with oscillatory growth zoning. However, Sb/(Sb + As) ratios of these grains scatter within a wide range, with the highest Sb contents corresponding to increased Bi, Se and Ag contents. This supports previous observations [56] that increasing As contents are coupled with decreasing Ag contents in tetrahedrite-group minerals. The oscillatory zoning of As–Sb and Fe–Zn as well as the substitution of Cu by Ag may indicate the physico-chemical—most probably temperature—changes during the crystallization of tetrahedrite-group minerals [28]. The observed ratios of Sb/(Sb + As) and Fe/(Fe + Zn) correspond to the data ranges of data presented by Marushchenko et al. [27] from the Baimka Cu–Mo–Au porphyry ore system. Mineral chemical analyses on epithermal tetrahedrite-group minerals were reported by Takács et al. [13]. Their data show that all generations of high sulfidation (HS) epithermal tetrahedrite-group minerals are dominated by Cu and Ag, while Zn and Fe are generally low (Figure 10). HS mineralization is characterized by higher Te and Bi contents as well, while intermediate sulfidation (IS) epithermal tetrahedrite group mineral compositions overlap with the porphyry–skarn–CAR field (Figure 9). IS and CAR data are generally overlapping, though Te is less abundant in the CAR mineralization compared to the IS tetrahedrite-group minerals.

4.5. Sulfosalts

The distribution of sulfosalts with various compositions in the mineralized system is not necessarily conclusive. Lead-rich, or Pb-dominated, sulfosalts were mostly found in the carbonate-replacement mineralization (Figure 11), although some Pb–Cu–Bi sulfosalts

are present in late carbonate veins with sphalerite–galena dominant mineral composition of the porphyry mineralization, too. These late veins are therefore petrographically and geochemically linked to the ore forming fluids of the CAR mineralization. In skarn samples, Bi and Cu–Bi sulfosalts and sulfotellurides were found predominantly, while Pb occurs only in galena, not in the form of sulfosalts. The most abundant sulfosalt mineral observed in the deep-seated orebodies was aikinite and transitional compositions within the aikinite–bismuthinite homologous series [49], occurring dominantly in the CAR mineralization type. Occurrence of Pb-bearing sulfosalts mainly in the distal parts of the deep-seated orebodies may be connected to the large scale of distribution of elements in the whole mineral system. The same zonation is also visible in the distribution of ore-forming elements in the skarn mineralization, as well as the zonal occurrence of the different ore types [57]. An alternative explanation for the preferential occurrence of Pb within the carbonate-replacement mineralization can be the partly sedimentary origin of Pb in this mineralization type. Tellurium sulfosalt minerals occur throughout the mineralized system. Tetradymite, hessite, and emplectite occur in all five mineralization types within the mineralized Recsk complex.

4.6. Behavior of Selenium

In the case of molybdenite, galena, and tetrahedrite-group minerals, a major trend was observed of relatively increasing Se concentrations towards the CAR mineralization. Even though this trend is not highlighted by any kind of statistically sound correlation of Se with other elements within the studied mineral grains, the question of temperature or distance-dependent behavior of Se within the whole porphyry hydrothermal system may be raised similarly to the suggestion of Keith et al. [57] for pyrite. The lack of correlation of Se with other elements may be due to the relatively low number of analyses, or further controlling factors, like partitioning of Se between co-precipitating minerals, which were not studied in detail in this study.

5. Conclusions

The magmatic–hydrothermal system at Recsk includes porphyry-style, skarn, and distal carbonate-replacement-type mineralization at subvolcanic levels. The systematic mineralogical and textural analyses of sulfide minerals from the various types of ores revealed that the trace element contents of molybdenite, galena, and tetrahedrite-group minerals can be useful as proximity indicators and for discriminating mineralization types in this porphyry-intrusion-related magmatic–hydrothermal system. The Re content of molybdenite decreases from the central porphyry Cu mineralization towards the more distal skarn and carbonate replacement type of mineralization in the country rocks. In galena and tetrahedrite-group minerals, Ag, Bi, and Se contents increase within the more distal mineralization types. This is also coupled with increasing Sb and Zn contents in the tetrahedrite-group minerals. Thus, Re in molybdenite, and Ag, Bi, and probably Se in galena, as well as Sb, Zn, Ag, and Bi in tetrahedrite-group minerals, may be applied for differentiating mineralization types and as vectors towards the porphyry intrusion within a porphyry–copper-type mineral system.

Compositional variation of sphalerite was found to be of limited use for fingerprinting or vectoring purposes within the Recsk ore complex based on EPMA measurements. In every ore type, anomalous behavior of Mn, Fe, Zn in sphalerite with “chalcopyrite disease” was detected. However, sphalerite crystals that have been co-precipitated with pyrite and without “chalcopyrite disease” in the carbonate replacement type ore show obvious linear correlations between these elements. Kesterite inclusions with similar texture to the “chalcopyrite disease” within sphalerite were also found in the latter type of ore. Any secondary replacement phenomenon occurring in sphalerite (chalcopyrite or kesterite “disease”) makes the sphalerite data absolutely inconsistent, limiting its value for fingerprinting, thermobarometry, or vectoring.

Galena replacement by myrmecitic–lamellar aikinite was also observed. The abundant occurrence of these replacement textures within an approximately 2 km wide zone in the distal part of the porphyry system indicates a widespread distal hydrothermal Cu-mobilization event. This could be caused either by remobilization of some central, Cu-rich, mineralized body or the distal presence of primary Cu-bearing ore-forming hydrothermal fluids.

Supplementary Materials: The following supporting information can be downloaded at: <https://www.mdpi.com/article/10.3390/min14090956/s1>, sum_EPMA_data_minerals.xlsx with all measurement data.

Author Contributions: Conceptualization, M.B. and F.M.; sampling, F.M.; methodology, M.B., M.F., J.G.R. and G.B.K.; software, A.V.; formal analysis, A.V.; investigation, M.B., M.F., M.H. and G.B.K.; resources, J.G.R. and G.B.K.; data curation, A.V. and M.B.; writing—original draft preparation, M.B.; writing—review and editing M.H., J.G.R., G.B.K. and F.M.; visualization, A.V.; supervision, F.M.; project administration, F.M.; funding acquisition, F.M. and J.G.R. All authors have read and agreed to the published version of the manuscript.

Funding: This research was supported by the Central European Exchange Programme for University Studies (CEEPUS) program.

Data Availability Statement: The original contributions presented in the study are included in the article/Supplementary Material, further inquiries can be directed to the corresponding author/s.

Acknowledgments: This research is a part of the PhD thesis of the first author supervised by F. Molnár and T.G. Weiszbürg at the Department of Mineralogy, Eötvös Loránd University. The research was supported by a scholarship provided by the Earth Science Doctoral School of the Eötvös Loránd University. The Eugen F. Stumpfl Electron Microprobe Laboratory at Montanuniversität Leoben provided invaluable support to this research in the frame of the Central European Exchange Programme for University Studies (CEEPUS). The work of G. B. Kiss is supported by the János Bolyai Research Scholarship awarded by the Hungarian Academy of Sciences and the ÚNKP-23-5 New National Excellence Program of the Ministry for Culture and Innovation from the source of the National Research, Development, and Innovation Fund. The Auro-Science Consulting Ltd., Hungary also supported the studies by providing access to a desktop scanning electron microscope that was invaluable for high-resolution petrography and selection of mineral phases for electron microprobe analyses.

Conflicts of Interest: The authors declare no conflicts of interest.

References

1. John, D.A.; Taylor, R.D. By-Products of Porphyry Copper and Molybdenum Deposits. In *Rare Earth and Critical Elements in Ore Deposits*; Verplanck, P.L., Hitzman, M.W., Eds.; Reviews in Economic Geology; Society of Economic Geologists: Littleton, CO, USA, 2016; Volume 18, Chapter 7; pp. 137–164. ISBN 9781629490922. [[CrossRef](#)]
2. Elshkaki, A.; Graedel, T.E.; Ciacci, L.; Reck, B. Copper Demand, Supply, and Associated Energy Use to 2050. *Glob. Environ. Chang.* **2016**, *39*, 305–315. [[CrossRef](#)]
3. Seck, G.S.; Hache, E.; Bonnet, C.; Simoën, M.; Carcanague, S. Copper at the Crossroads: Assessment of the Interactions between Low-Carbon Energy Transition and Supply Limitations. *Resour. Conserv. Recycl.* **2020**, *163*, 105072. [[CrossRef](#)] [[PubMed](#)]
4. Cseh-Németh, J. Deep-seated base metal ore occurrence of Recksk: Geological pattern of ore accumulation. *Bull. Hung. Geol. Soc.* **1975**, *105*, 692–708. (In Hungarian)
5. Csillag, J. Rocks transformed upon magmatic effect in the Recksk area. *Bull. Hung. Geol. Soc.* **1975**, *105*, 646–671. (In Hungarian)
6. Csongrády, J. Characterization of the deep-seated base metal ore mineralization of Recksk on the basis of ore-microscopic analyses. *Bull. Hung. Geol. Soc.* **1975**, *105*, 672–691. (In Hungarian)
7. Baksa, C. Genetic Aspects of the Recksk Mineralized Complex, Hungary. In *Geology and Metallogeny of Copper Deposits*; Conference Paper; Springer: Berlin/Heidelberg, Germany, 1986; pp. 280–290. [[CrossRef](#)]
8. Gatter, I.; Molnár, F.; Földessy, J.; Zelenka, T.; Kiss, J.; Szebényi, G. High- and low-sulfidation epithermal mineralization of the Mátra Mountains, Northeast Hungary. In *Epithermal Mineralization of the Western Carpathians*; Molnár, F., Lexa, J., Hedenquist, J., Eds.; Society of Economic Geologists Guidebook Series; Society of Economic Geologists: Littleton, CO, USA, 1999; Volume 31, pp. 155–179.

9. Zelenka, T.; Szebényi, G. Exploration history of the base metal deposit at Recsk deep levels. In *Mineral Exploration in Hungary during the XXth Century*; Miskolc-Rudabánya; Szakáll, S., Morvai, G., Eds.; 2002; pp. 169–198. Available online: https://library.hungaricana.hu/hu/collection/muze_szak_asva_kozlemenyek/ (accessed on 20 September 2024).
10. Molnár, F. The Cu-Au-Ag-Zn-Pb ore complex at Recsk, Hungary: A uniquely preserved and explored porphyry-skarn-epithermal system in the Palaeogene magmatic belt of the Alp-Carpathian-Dinaride system. In *Proceedings of the Ninth Biennial SGA Symposium, Dublin, Ireland, 20–23 August 2007*; Volume 1, pp. 153–157.
11. Molnár, F.; Jung, P.; Kupi, L.; Pogány, A.; Vágó, E.; Viktorik, O.; Pécskay, Z. Epithermal Zones of the Porphyry-Skarn-Epithermal Ore Complex at Recsk. In *Recsk and Lahóca—Geology of the Paleogene Ore Complex*; Földessy, J., Hartai, É., Eds.; Publications of the University of Miskolc, Series A, Mining; University of Miskolc: Miskolc, Hungary, 2008; Volume 73, pp. 99–128.
12. Földessy, J.; Hartai, É. *Recsk and Lahóca: Geology of the Paleogene Ore Complex*; Publications of the University of Miskolc, Series A, Mining; University of Miskolc: Miskolc, Hungary, 2008; Volume 73.
13. Takács, Á.; Molnár, F.; Turi, J.; Mogessie, A.; Menzies, J.C. Ore Mineralogy and Fluid Inclusion Constraints on the Temporal and Spatial Evolution of a High-Sulfidation Epithermal Cu-Au-Ag Deposit in the Recsk Ore Complex, Hungary. *Econ. Geol.* **2017**, *112*, 1461–1481. [[CrossRef](#)]
14. Altenberger, F.; Raith, J.G.; Bakker, R.J.; Zarsavandi, A. The Chah-Mesi Epithermal Cu-Pb-Zn-(Ag-Au) Deposit and Its Link to the Meiduk Porphyry Copper Deposit, SE Iran: Evidence from Sulfosalt Chemistry and Fluid Inclusions. *Ore Geol. Rev.* **2022**, *142*, 104732. [[CrossRef](#)]
15. Cooke, D.R.; Agnew, P.; Hollings, P.; Baker, M.; Chang, Z.; Wilkinson, J.J.; White, N.C.; Zhang, L.; Thompson, J.; Gemmill, J.B.; et al. Porphyry indicator minerals (PIMS) and porphyry vectoring and fertility tools (PVFTS)—indicators of mineralization styles and recorders of hypogene geochemical dispersion halos. In *Proceedings of the Decennial Mineral Exploration Conferences, Toronto, ON, Canada, 22–25 October 2017*; pp. 457–470.
16. Cooke, D.R.; Agnew, P.; Hollings, P.; Baker, M.; Chang, Z.; Wilkinson, J.J.; Ahmed, A.; White, N.C.; Zhang, L.; Thompson, J.; et al. Recent Advances in the Application of Mineral Chemistry to Exploration for Porphyry Copper–Gold–Molybdenum Deposits: Detecting the Geochemical Fingerprints and Footprints of Hypogene Mineralization and Alteration. *Geochem. Explor. Environ. Anal.* **2020**, *20*, 176–188. [[CrossRef](#)]
17. Sykora, S.; Cooke, D.R.; Meffre, S.; Stephanov, A.S.; Gardner, K.; Scott, R.; Selley, D.; Harris, A.C. Evolution of Pyrite Trace Element Compositions from Porphyry-Style and Epithermal Conditions at the Lihir Gold Deposit: Implications for Ore Genesis and Mineral Processing. *Econ. Geol.* **2018**, *113*, 193–208. [[CrossRef](#)]
18. Börner, F.; Keith, M.; Smith, D.J.; Barry, T.L.; Neumann, T.; Klemm, R. Fingerprinting Fluid Evolution by Trace Elements in Epithermal Pyrite, Vatukoula Au-Te Deposit, Fiji. *Ore Geol. Rev.* **2021**, *137*, 104314. [[CrossRef](#)]
19. Cave, B.; Lilly, R.; Barovich, K. Textural and Geochemical Analysis of Chalcopyrite, Galena and Sphalerite across the Mount Isa Cu to Pb-Zn Transition: Implications for a Zoned Cu-Pb-Zn System. *Ore Geol. Rev.* **2020**, *124*, 103647. [[CrossRef](#)]
20. Cioacă, M.E.; Munteanu, M.; Qi, L.; Costin, G. Trace Element Concentrations in Porphyry Copper Deposits from Metaliferi Mountains, Romania: A Reconnaissance Study. *Ore Geol. Rev.* **2014**, *63*, 22–39. [[CrossRef](#)]
21. Keith, M.; Haase, K.M.; Chivas, A.R.; Klemm, R. Phase Separation and Fluid Mixing Revealed by Trace Element Signatures in Pyrite from Porphyry Systems. *Geochim. Cosmochim. Acta* **2022**, *329*, 185–205. [[CrossRef](#)]
22. Kullerud, G. The FeS-ZnS system—A geological thermometer. *Nor. Geol. Tidsskrift* **1953**, *32*, 62–147.
23. Frenzel, M.; Hirsch, T.; Gutzmer, J. Gallium, Germanium, Indium, and Other Trace and Minor Elements in Sphalerite as a Function of Deposit Type—A Meta-Analysis. *Ore Geol. Rev.* **2016**, *76*, 52–78. [[CrossRef](#)]
24. Barton, I.F.; Rathkopf, C.A.; Barton, M.D. Rhenium in Molybdenite: A Database Approach to Identifying Geochemical Controls on the Distribution of a Critical Element. *Min. Met. Explor.* **2020**, *37*, 21–37. [[CrossRef](#)]
25. Ciobanu, C.L.; Cook, N.J.; Kelson, C.R.; Guerin, R.; Kalleske, N.; Danyushevsky, L. Trace Element Heterogeneity in Molybdenite Fingerprints Stages of Mineralization. *Chem. Geol.* **2013**, *347*, 175–189. [[CrossRef](#)]
26. Terada, K.; Osaki, S.; Ishihara, S.; Kiba, T. Distribution of Rhenium in Molybdenites from Japan. *Geochem. J.* **1971**, *4*, 123–141. [[CrossRef](#)]
27. Marshchenko, L.I.; Baksheev, I.A.; Nagornaya, E.V.; Chitalin, A.F.; Nikolaev, Y.N.; Vlasov, E.A. Compositional Evolution of the Tetrahedrite Solid Solution in Porphyry-Epithermal System: A Case Study of the Baimka Cu-Mo-Au Trend, Chukchi Peninsula, Russia. *Ore Geol. Rev.* **2018**, *103*, 21–37. [[CrossRef](#)]
28. Sack, R.O. Fahlore Thermochemistry: Gaps inside the (Cu,Ag)₁₀(Fe,Zn)₂(Sb,As)₄S₁₃ Cube. *Petrology* **2017**, *25*, 498–515. [[CrossRef](#)]
29. Benedek, K. Paleogene Igneous Activity along the Easternmost Segment of the Periadriatic-Balaton Lineament. *Acta Geol. Hung.* **2002**, *45*, 359–371. [[CrossRef](#)]
30. Exner, C. *Die Geologische Position der Magmatite des Periadriatischen Lineamentes*; Geologische Bundesanstalt: Vienna, Austria, 1976; pp. 3–64.
31. Földessy, J.; Zelenka, T.; Benedek, K.; Pécskay, Z.; Mádai, F. The Recsk Paleogene magmatism in a regional context. In *Recsk and Lahóca—Geology of the Paleogene Ore Complex*; Földessy, J., Hartai, É., Eds.; Publications of the University of Miskolc, Series A, Mining; University of Miskolc: Miskolc, Hungary, 2008; Volume 73, pp. 7–20.
32. Raith, J.G.; Hutter, F.; Altenberger, F.; Weilbold, J.; Auer, C.; Krause, J.; Berndt, J.; Neinavaie, H. Polymetallic Tungsten Skarn Mineralisation Related to the Periadriatic Intrusion at Lienzer Schlossberg, East Tyrol, Austria. *Austrian J. Earth Sci.* **2024**, *117*, 87–112. [[CrossRef](#)]

33. Arató, R.; Dunkl, I.; Takács, Á.; Szebényi, G.; Gerdes, A.; Von Eynatten, H. Thermal Evolution in the Exhumed Basement of a Stratovolcano: Case Study of the Miocene Mátra Volcano, Pannonian Basin. *J. Geol. Soc.* **2018**, *175*, 820–835. [[CrossRef](#)]
34. Zelenka, T.; Markó, B. Comparative results of exploratory shaft-sinking and tunnel-driving and exploratory deep drilling at the Recsk ore deposit. *Bull. Hung. Geol. Soc.* **1979**, *109*, 469–477. (In Hungarian)
35. Baksa, C. The genetic framework of the Recsk ore genesis. *Acta Mineralogica-Petrogr. Szeged.* **1983**, *XXVI/1*, 87–97.
36. Kovács, S.; Gecse, Z.; Pelikán, P.; Zelenka, T.; Szebényi, G.; Szabó, I. Upper Triassic conodonts from deep boreholes of the Recsk–Dárnó area: New data on the geology of its pre-Cenozoic basement. *Bull. Hung. Geol. Soc.* **2013**, *143*, 29–46. (In Hungarian)
37. Molnár, F.; Gatter, I.; Zelenka, T.; Pécskay, Z.; Bernadett, B. Metallogeny of Paleogene and Neogene Volcanic Belts in Hungary. In Proceedings of the 7th Biannual SGA Meeting, Balkema, Rotterdam, The Netherlands, 24–28 August 2003; Volume 2, pp. 1205–1208.
38. Földessy, J.; Seres-Hartai, É.; Szebényi, G. Distribution of Gold Mineralization in the Recsk Ore Complex, NE Hungary. *Acta Geol. Hung.* **2004**, *47*, 247–258. [[CrossRef](#)]
39. Singer, D.A.; Berger, V.I.; Moring, B.C. *Porphyry Copper Deposits of the World: Database and Grade and Tonnage Models*; USGS Reports; USGS: Reston, VA, USA, 2008.
40. Török, K.; Gyuricza, G.; Szeiler, R.B.; Füged, U.; Gál, N.; Gáspár, E.; Gulyás, Á.; Horváth, Z.; Kerékgyártó, T.; Korbély, B.; et al. *Complex Vulnerability and Loadability Assessment Report to Recsk II. Copper Ore Proposed Area for Concession*; Hungarian Office for Mining and Geology: Budapest, Hungary, 2016. Available online: https://mbfsz.gov.hu/sites/default/files/file/2018/07/06/recsk_ii_eng.pdf (accessed on 20 September 2024).
41. Földessy, J.; Szebényi, G. The mineralizations of the the Recsk deeps and Lahóca—Short geological overview. In *Recsk and Lahóca—Geology of the Paleogene Ore Complex*; Földessy, J., Hartai, É., Eds.; Publications of the University of Miskolc, Series A, Mining; University of Miskolc: Miskolc, Hungary, 2008; Volume 73, pp. 85–98.
42. R Core Team. *R: A Language and Environment for Statistical Computing*; R Foundation for Statistical Computing: Vienna, Austria, 2003; Available online: <https://www.r-project.org> (accessed on 20 September 2024).
43. Sillitoe, R.H. Porphyry Copper Systems. *Econ. Geol.* **2010**, *105*, 3–41. [[CrossRef](#)]
44. Ramdohr, P. *Ore Minerals and Their Intergrowths*, 2nd ed.; Pergamon Press: Oxford, UK, 1980.
45. Barton, P.B.; Bethke, P.M. Chalcopyrite Disease in Sphalerite: Pathology and Epidemiology. *Am. Mineral.* **1987**, *72*, 451–467.
46. Foord, E.E.; Shawe, D.R. The Pb-Bi-Ag-Cu-(Hg) chemistry of galena and some associated sulfosalts: A review and some new data from Colorado, California and Pennsylvania. *Can. Mineral.* **1989**, *27*, 363–382.
47. Blackburn, W.H.; Schwendeman, J.F. Trace Element Substitution in Galena. *Can. Miner.* **1977**, *15*, 365–373.
48. Cook, N.J.; Ciobanu, C.L.; Pring, A.; Skinner, W.; Shimizu, M.; Danyushevsky, L.; Saini-Eidukat, B.; Melcher, F. Trace and Minor Elements in Sphalerite: A LA-ICPMS Study. *Geochim. Cosmochim. Acta* **2009**, *73*, 4761–4791. [[CrossRef](#)]
49. Moëlo, Y.; Makovicky, E.; Mozgova, N.N.; Jambor, J.L.; Cook, N.; Pring, A.; Paar, W.; Nickel, E.H.; Graeser, S.; Karup-Møller, S.; et al. Sulfosalt Systematics: A Review. Report of the Sulfosalt Sub-Committee of the IMA Commission on Ore Mineralogy. *Eur. J. Mineral.* **2008**, *20*, 7–62. [[CrossRef](#)]
50. Pasava, J.; Svojtka, M.; Veselovský, F.; Ďurišová, J.; Ackerman, L.; Pour, O.; Drábek, M.; Halodová, P.; Haluzová, E. Laser Ablation ICPMS Study of Trace Element Chemistry in Molybdenite Coupled with Scanning Electron Microscopy (SEM)—An Important Tool for Identification of Different Types of Mineralization. *Ore Geol. Rev.* **2016**, *72*, 874–895. [[CrossRef](#)]
51. Renock, D.; Becker, U. A First Principles Study of Coupled Substitution in Galena. *Ore Geol. Rev.* **2011**, *42*, 71–83. [[CrossRef](#)]
52. George, L.; Cook, N.J.; Cristiana, C.; Wade, B.P. Trace and Minor Elements in Galena: A Reconnaissance LA-ICP-MS Study. *Am. Mineral.* **2015**, *100*, 548–569. [[CrossRef](#)]
53. Craig, J.R. Phase Relations and Mineral Assemblages in the Ag-Bi-Pb-S System. *Miner. Depos.* **1967**, *1*, 278–306. [[CrossRef](#)]
54. Yin, S.; Wirth, R.; He, H.; Ma, C.; Pan, J.; Xing, J.; Xu, J.; Fu, J.; Zhang, X.N. Replacement of Magnetite by Hematite in Hydrothermal Systems: A Refined Redox-Independent Model. *Earth Planet. Sci. Lett.* **2022**, *577*, 117282. [[CrossRef](#)]
55. Bortnikov, N.S.; Dobrovol'skaya, M.G.; Genkin, A.D.; Naumov, V.B.; Shapenko, V.V. Sphalerite-Galena Geothermometers: Distribution of Cadmium, Manganese, and the Fractionation of Sulfur Isotopes. *Econ. Geol.* **1995**, *90*, 155–180. [[CrossRef](#)]
56. Ebel, D.S.; Sack, R. Arsenic-Silver Incompatibility in Fahlore. *Mineral. Mag.* **1991**, *55*, 521–528. [[CrossRef](#)]
57. Keith, M.; Smith, D.J.; Jenkin, G.R.T.; Holwell, D.A.; Dye, M.D. A Review of Te and Se Systematics in Hydrothermal Pyrite from Precious Metal Deposits: Insights into Ore-Forming Processes. *Ore Geol. Rev.* **2018**, *96*, 269–282. [[CrossRef](#)]

Disclaimer/Publisher's Note: The statements, opinions and data contained in all publications are solely those of the individual author(s) and contributor(s) and not of MDPI and/or the editor(s). MDPI and/or the editor(s) disclaim responsibility for any injury to people or property resulting from any ideas, methods, instructions or products referred to in the content.